

FFI RAPPORT

**MASTER OSCILLATOR/POWER AMPLIFIER
SYSTEM FOR OPTICAL PARAMETRIC
CONVERSION OF HIGH-ENERGY PULSES
FROM 1 TO 2 μ m**

NORDSETH Ørnulf

FFI/RAPPORT-2004/02159

**MASTER OSCILLATOR/POWER AMPLIFIER
SYSTEM FOR OPTICAL PARAMETRIC
CONVERSION OF HIGH-ENERGY PULSES
FROM 1 TO 2 μ m**

NORDSETH Ørnulf

FFI/RAPPORT-2004/02159

**FORSVARETS FORSKNINGSINSTITUTT
Norwegian Defence Research Establishment
P O Box 25, NO-2027 Kjeller, Norway**

FORSVARETS FORSKNINGSISTITUTT (FFI)
Norwegian Defence Research Establishment

UNCLASSIFIED

P O BOX 25
 NO-2027 KJELLER, NORWAY

SECURITY CLASSIFICATION OF THIS PAGE
 (when data entered)

REPORT DOCUMENTATION PAGE

1) PUBL/REPORT NUMBER FFI/RAPPORT-2004/02159	2) SECURITY CLASSIFICATION UNCLASSIFIED	3) NUMBER OF PAGES 60		
1a) PROJECT REFERENCE FFI-III/856	2a) DECLASSIFICATION/DOWNGRADING SCHEDULE -			
4) TITLE MASTER OSCILLATOR/POWER AMPLIFIER SYSTEM FOR OPTICAL PARAMETRIC CONVERSION OF HIGH-ENERGY PULSES FROM 1 TO 2 μ m				
5) NAMES OF AUTHOR(S) IN FULL (surname first) NORDSETH Ørnulf				
6) DISTRIBUTION STATEMENT Approved for public release. Distribution unlimited. (Offentlig tilgjengelig)				
7) INDEXING TERMS <table style="width: 100%; border-collapse: collapse;"> <tr> <td style="width: 50%; vertical-align: top;"> IN ENGLISH: <ul style="list-style-type: none"> a) Optical resonators b) Optical parametric oscillators c) Optical frequency conversion d) Beam quality e) High energy </td> <td style="width: 50%; vertical-align: top;"> IN NORWEGIAN: <ul style="list-style-type: none"> a) Optiske resonatorer b) Optiske parametriske oscillatorer c) Optisk frekvenskonvertering d) Strålekvalitet e) Høy energi </td> </tr> </table>			IN ENGLISH: <ul style="list-style-type: none"> a) Optical resonators b) Optical parametric oscillators c) Optical frequency conversion d) Beam quality e) High energy 	IN NORWEGIAN: <ul style="list-style-type: none"> a) Optiske resonatorer b) Optiske parametriske oscillatorer c) Optisk frekvenskonvertering d) Strålekvalitet e) Høy energi
IN ENGLISH: <ul style="list-style-type: none"> a) Optical resonators b) Optical parametric oscillators c) Optical frequency conversion d) Beam quality e) High energy 	IN NORWEGIAN: <ul style="list-style-type: none"> a) Optiske resonatorer b) Optiske parametriske oscillatorer c) Optisk frekvenskonvertering d) Strålekvalitet e) Høy energi 			
THESSAURUS REFERENCE:				
8) ABSTRACT <p>The topic of this work has been to convert the wavelength of a high energy 1 μm Nd:YAG laser to 2 μm. In order to achieve high efficiency without compromising beam quality, a two-stage system was designed and implemented in the laboratory. The first stage was an optical parametric oscillator (OPO) that converted a narrow 1 μm beam with about 8 mJ energy to a 2 μm signal of relatively high quality. An optical parametric amplifier (OPA) pumped with up to 500 mJ formed the second stage and used the OPO signal as input. Both stages of the master oscillator/power amplifier (MOPA) system were based on the nonlinear crystal KTiOPO₄ (KTP). With 500 mJ pump energy, different OPA configurations produced up to 138 mJ signal energy with $M^2 \approx 2.3$. Numerical simulations of the MOPA configuration gave good agreement with the experimental results.</p>				
9) DATE 2004-08-05	AUTHORIZED BY This page only Johnny Bardal	POSITION Director		

UNCLASSIFIED

SECURITY CLASSIFICATION OF THIS PAGE
 (when data entered)

PREFACE

This report is a modification of my master's thesis submitted to the Norwegian University of Science and Technology (NTNU) June 2004. The master assignment was a continuation of a project assignment carried out at FFI in the autumn of 2003.

I would like to express my gratitude towards my supervisors at FFI, Gunnar Arisholm and Gunnar Rustad, for valuable assistance during the work. I would also like to thank other members of the Electro-optics group at FFI from whom I have received help and the Machine shop employees that made the parts for the OPO resonator.

CONTENTS

	Page
PREFACE	5
1 INTRODUCTION	9
2 THEORY	10
2.1 Nonlinear polarization	10
2.2 Second order nonlinear interactions	11
2.2.1 Birefringent phase-matching	13
2.2.2 Tuning	14
2.2.3 Walk-off	14
2.2.4 Acceptance angles	15
2.3 Optical parametric oscillator (OPO)	17
2.3.1 OPO performance parameters	17
2.3.2 Power scaling	18
2.3.3 Master oscillator/power amplifier	19
2.4 Pump characteristics	20
2.4.1 The pulse	20
2.4.2 The intensity distribution	21
2.4.3 Beam quality	22
3 EXPERIMENTS	23
3.1 Preliminary experiment	23
3.1.1 Ring OPO	24
3.1.2 Linear OPO	26
3.1.3 OPA pump paths	27
3.1.3.1 Relay-imaging telescope	28
3.1.3.2 Expansion telescopes	30
3.1.4 OPO pump pulse characterization	31
3.1.5 Relay-imaging telescope in the OPO pump path	31
3.2 The MOPA configuration scaled to higher energy	34
3.2.1 OPA pump energies up to 400 mJ	34
3.2.2 OPA pump energies up to 500 mJ and multiple OPA crystals	37
3.3 Summary of experiments	39
3.4 Instrumentation	41
4 SIMULATIONS	42
4.1 The simulation model	42
4.2 Previous simulations	42

4.3	New simulations	44
4.3.1	Linear OPO	44
4.3.2	The MOPA configuration	45
5	DISCUSSION	49
5.1	Optimization of the conversion efficiency	49
5.2	Optimization of the beam quality	50
5.3	General comments on the MOPA system	51
5.4	Deviations between lab measurements and simulations	52
5.5	Plans ahead	52
6	CONCLUSION	53
APPENDICES		54
A	DETERMINATION OF TIME DELAY IN THE 2 μm DETECTOR	54
B	PHOTOGRAPHS OF THE IMPLEMENTATION IN THE LAB	55
C	LENS COMBINATION FORMULAS	55
D	TRANSMISSION CHARACTERISTICS OF THE OPO MIRRORS	57
References		59

MASTER OSCILLATOR/POWER AMPLIFIER SYSTEM FOR OPTICAL PARAMETRIC CONVERSION OF HIGH-ENERGY PULSES FROM 1 TO 2 μm

1 INTRODUCTION

The 3-5 μm and 8-12 μm wavelength ranges are important in applications that require good transmission in the atmosphere, as seen from Figure 1.1.

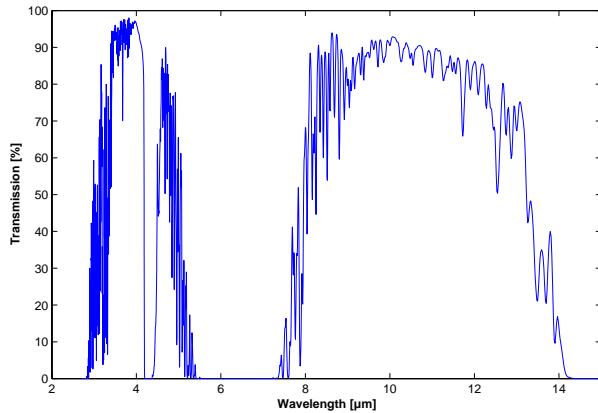


Figure 1.1 Horizontal transmittance of electromagnetic radiation through a kilometer of the atmosphere as a function of wavelength. The relative humidity is 50 % and the temperature is 20 °C. Dipole molecules in the atmosphere absorb photons at certain frequencies, leading to poor transmission of electromagnetic radiation. However, the transmittance is fairly high in two distinct wavelength intervals, commonly referred to as the 3-5 μm and 8-12 μm windows.

For this reason, there is also a strong interest in lasers that operate in these wavelength ranges. However, except for the CO₂ laser, which covers part of the 8-12 μm range, there is a lack of practical, high-power lasers in these ranges. Moreover, most lasers have a very limited tuning range because their radiation originates from transitions between specific energy levels.

These problems can be solved by nonlinear optical frequency conversion. A nonlinear crystal driven by an intense laser beam (called the pump beam) at one wavelength can provide gain for signal beams at longer wavelengths. Such a device is called an optical parametric amplifier (OPA) [1]. If an OPA is placed inside an optical resonator it can give rise to self-sustained oscillation, just like the amplifying medium in a conventional laser. Such a device is called an optical parametric oscillator (OPO) [2]. An important advantage compared to conventional lasers is that the gain wavelength of the OPA is not tied to a transition between fixed energy levels, so the output wavelength can be chosen with much more freedom, and it can even be tunable over a wide range.

OPOs have been demonstrated successfully both in the 3-5 μm and the 8-12 μm wavelength ranges. However, the generation of suitable pump beams remains a challenge. High-energy

lasers with wavelength near 1 μm are efficient and technologically mature, but the nonlinear crystals most suitable for the 3-5 μm and 8-12 μm ranges are not transparent for 1 μm light. On the other hand, they can be pumped by 2 μm , but high-energy lasers for this wavelength are not readily available. One option for producing the 2 μm pump beam is to start from a 1 μm laser and convert to 2 μm by another OPO [3, 4]. The topic of the present work is to scale this approach to higher energy.

Due to the limited damage threshold of nonlinear crystals, frequency conversion of high-energy laser pulses requires wide beam diameters in order to avoid high concentration of energy. Wide pump beams give poor suppression of higher order transversal modes in an OPO, making it difficult to achieve high beam quality, without compromising conversion efficiency. We address this challenge by implementing a two-stage master oscillator/power amplifier system.

Chapter 2 briefly reviews the theory of nonlinear polarization, second order nonlinear interaction, optical parametric oscillator (OPO), and pump characteristics and serves as background needed to describe the implemented configuration. Chapter 3 describes the experimental setup and the measurements made in the laboratory. Chapter 4 presents the numerical model and summarizes the results of the simulations. Finally, Chapter 5 discusses the results and proposes potential improvements of the configuration.

2 THEORY

Much of the contents of the theory chapter are based on suggestions and explanations from my supervisors. Each of the subchapters presents fundamental topics of the operation of the implemented system.

2.1 Nonlinear polarization

When an electromagnetic wave propagates in a dielectric medium the electric field (\vec{E}) gives rise to a polarization (\vec{P}). For a linear dielectric medium the polarization is given by

$$\vec{P} = \epsilon_0 \chi^{(1)} \vec{E}, \quad (2.1)$$

where ϵ_0 is the electric permittivity of free space and $\chi^{(1)}$ is the linear electric susceptibility of the medium.

For a nonlinear medium the relation between \vec{P} and \vec{E} is customarily written as the Taylor series [5]

$$\vec{P} = \epsilon_0 \left(\chi^{(1)} \vec{E} + \chi^{(2)} \vec{E}^2 + \chi^{(3)} \vec{E}^3 + \dots \right), \quad (2.2)$$

where $\chi^{(2)}$ and $\chi^{(3)}$ are the second- and third-order nonlinear optical susceptibility tensors, respectively. Generally, $\chi^{(n+1)} \ll \chi^{(n)}$, so unless the intensity is extremely high, the higher

order terms in (2.2) can be neglected if the second order nonlinear term, $\chi^{(2)}$, is nonzero. The second order susceptibility is often expressed by $d = \chi^{(2)}/2$.

Under conditions that will be discussed below, the nonlinear polarization terms can generate new waves and give rise to second harmonic generation (SHG), sum-frequency generation (SFG) and difference-frequency generation (DFG). DFG is of primary interest in this work, because this is the underlying process in the optical parametric oscillator (OPO).

2.2 Second order nonlinear interactions

SHG, SFG and DFG are often called parametric mixing. The term parametric means that energy is not absorbed from or supplied to the nonlinear process by the nonlinear medium. SFG and DFG are interactions of three beams with the angular frequencies ω_1 , ω_2 and ω_3 , where $\omega_1 + \omega_2 = \omega_3$. Assume an interaction of three plane waves in a steady state propagating in the z-direction with electric-field amplitudes

$$E_q = e_q \exp(-j(\omega_q t - k_q z)), \quad q = 1, 2, 3, \quad (2.3)$$

where e_q are the complex envelopes, $k_q = \omega_q n_q / c$ the wave numbers, n_q are the refractive indices, and c is the speed of light in vacuum. For simplicity, the amplitudes have been written as scalars. This is justified when each beam has a well-defined, fixed polarization. The equations that describe the evolution of the slowly varying complex amplitudes can be written as [6]

$$\frac{\delta e_1}{\delta z} = j \frac{\omega_1}{n_1 c} \chi_{\text{eff}} e_3 e_2^* \exp(j\Delta kz) \quad (2.4)$$

$$\frac{\delta e_2}{\delta z} = j \frac{\omega_2}{n_2 c} \chi_{\text{eff}} e_3 e_1^* \exp(j\Delta kz) \quad (2.5)$$

$$\frac{\delta e_3}{\delta z} = j \frac{\omega_3}{n_3 c} \chi_{\text{eff}} e_1 e_2 \exp(-j\Delta kz) \quad (2.6)$$

where χ_{eff} is the effective nonlinear susceptibility, which depends on the nonlinear tensor and the polarization directions of the interacting beams [7]. The quantity

$$\Delta k = k_3 - k_2 - k_1 \quad (2.7)$$

is called the phase-mismatch, and will be discussed below.

Equations (2.4)-(2.6) show that the three waves are coupled. The nonlinear polarization can thus transfer energy between the three waves in a process called three-wave mixing. When this effect is exploited to amplify a beam, the process is called optical parametric amplification (OPA). Energy from a pump wave, providing power to the amplification process, is transferred

to the signal and the third wave, called the idler. Idler, signal, and pump are referred to as waves 1, 2, and 3, respectively.

The Manley-Rowe relations [8]

$$\frac{d}{dz} \left(\frac{I_1}{\omega_1} \right) = \frac{d}{dz} \left(\frac{I_2}{\omega_2} \right) = - \frac{d}{dz} \left(\frac{I_3}{\omega_3} \right), \quad (2.8)$$

where $I_q = |e_q|^2$, can be derived from equations (2.4)-(2.6). Together with the frequency matching condition $\omega_1 + \omega_2 = \omega_3$, they imply a fixed total intensity in the parametric mixing process, i.e. no energy is lost.

The DFG process can also be looked upon as a three-photon interaction, in which an incoming photon of frequency ω_3 splits into two photons of frequencies ω_1 and ω_2 . The Manley-Rowe relation implies that the photon flux densities (number of photons/area) of the three waves satisfy

$$\frac{d\phi_1}{dz} = \frac{d\phi_2}{dz} = - \frac{d\phi_3}{dz}. \quad (2.9)$$

The energy exchange in the mixing process is efficient only if the nonlinear polarization drives the corresponding wave coherently over the length of the nonlinear crystal. This requires Δk to be small so that the exponential factors in equations (2.4)-(2.6) do not oscillate along the crystal. When $\Delta k = 0$, the mixing process is perfectly phase-matched. Then the relative phase of the three waves is constant while propagating through the nonlinear medium, so that the exchange of energy between the waves is efficient. For $\Delta k \neq 0$, there is a phase-mismatch which lowers the efficiency of the energy exchange. Figure 2.1 shows how the energy is periodically converted between the pump and the generated waves (signal and idler). Complete conversion is obtainable for phase-matched mixing (a), but not obtainable in the case of phase-mismatched mixing (b). Also, the oscillation of the periodical conversion is more rapid when the phase-mismatch is increased.

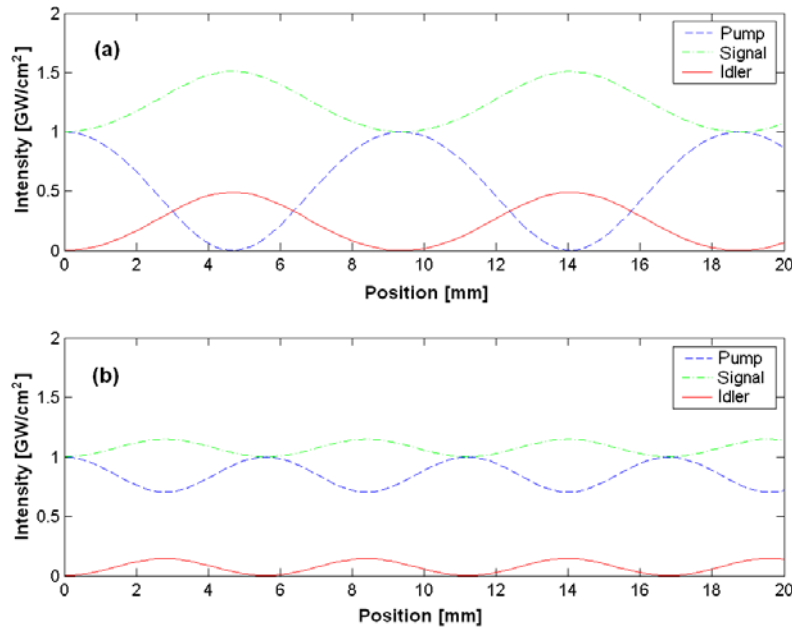


Figure 2.1 Evolution of the intensity in a nonlinear crystal with type 2 birefringent phase-matching for phase-matched mixing (a), $\Delta k \cdot L = 0$ and phase-mismatched mixing (b), $\Delta k \cdot L = 20$, where L is the length of the crystal. The signal and pump are incident with intensity of 1 GW/cm^2 , and the crystal length is 20 mm . The total intensity is constant in both cases, which agrees with the Manley-Rowe relations given in equation (2.8).

Ideal conversion occurs when the pump is totally depleted, so that all of its energy is transferred to the idler and signal. Referring back to Figure 2.1 (a), it can be seen that this happens approximately 4.5 mm into the nonlinear crystal. An undesirable effect occurs when energy flow in the mixing process changes direction so that the depleted wave is regenerated. This effect is called back-conversion and happens because the depleted wave must continue to participate in the three-wave mixing process in order to satisfy the wave conditions given in equation (2.4)-(2.6). Back-conversion of the pump is apparent in the region between 4.5 and 9 mm in the crystal in Figure 2.1 (a). It is obvious from the figure that the interaction length of the waves in the nonlinear medium is a parameter that makes it possible to control the back-conversion. For example, choosing a crystal of length 4.5 mm instead of 20 mm in case (a) will minimize back-conversion. The back-conversion is also dependent on the intensity of the pump and the oscillation period of the conversion becomes shorter with higher intensities. Ideally, one should therefore use a pump beam with a uniform intensity distribution to avoid the occurrence of back-conversion in the parts of the beam where the intensity deviates from the average value

2.2.1 Birefringent phase-matching

The phase-mismatch given in equation (2.7) can be rewritten as

$$\Delta k = (n_3\omega_3 - n_2\omega_2 - n_1\omega_1)/c = 0. \quad (2.10)$$

It follows that in an isotropic medium with normal dispersion, where ($n_3 > n_2, n_1$), phase-matching cannot be satisfied. However, second order nonlinear materials are usually

birefringent, meaning that the refractive index (n) is dependent on the direction of polarization of the beam. In these materials, the dispersion can be compensated and makes it possible to achieve phase-matching by a proper choice of polarization.

For a given propagation direction there are a fast and a slow mode. If the pump has the fast polarization, phase-matching can be achieved in certain propagation directions in the birefringent medium for different combinations of polarizations for the idler and signal. Birefringent phase-matching can therefore be classified as type 1, 2 and 3 depending on the polarization types of the interacting waves. The classification is summarized in Table 2.1. [6]

Type	ω_1	ω_2	ω_3
1	Slow	Slow	Fast
2	Fast	Slow	Fast
3	Slow	Fast	Fast

Table 2.1 Types of birefringent phase-matching.

In some parts of literature, “type 2” is used to describe both type 2 and type 3 in Table 2.1.

2.2.2 Tuning

Because the wavelength for which the phase-matching condition holds is dependent on the propagation direction, the OPA can be tuned by rotating the crystal. Tuning made in an OPO while the wavelength of the pump is kept constant, will result in the signal and idler wavelengths being changed to adapt to the new phase-matching conditions. Changing the temperature or applying an electric field across the crystal can also achieve tuning. These latter two techniques change the birefringence of the crystal. However, crystal rotation is most common because it allows a greater tuning range.

2.2.3 Walk-off

For a wave propagating in a birefringent medium, the Poynting vector (S) and the wave vector (k) are in general not parallel, implying that the transverse intensity distribution of the wave walks away from its propagation direction. This phenomenon is called walk-off. Both the orientation of the polarization and the direction of the wave relative to the crystal axes determine the angle between the Poynting vector and the wave vector, referred to as the walk-off angle.

Interacting waves with different polarizations not parallel to the crystal axes will have different walk-off angles. These deflections in different directions, due to walk-off, limit the effective interaction length for beams with small diameter and affect the beam profile. By the use of two crystals, orientated so that the walk-off in one crystal is opposite to the other, the problem with walk-off can be reduced. This is called walk-off compensation and is often utilized in OPAs and OPOs. There are different ways to orientate the second crystal in order to obtain walk-off compensation. To achieve efficient conversion the two crystals must be orientated to have the same sign of effective nonlinearity d_{eff} . Two factors determine the sign of d_{eff} for a particular crystal and mixing process. One is the cut of the crystal relative to the crystallographic axes

and the other is the orientation of the crystal. In the case with identically cut crystals and an odd number of extraordinary polarized waves (as used in this work) in the interaction, the second crystal must be rotated around the vertical axis for efficient conversion, as shown in Figure 2.2 (a).

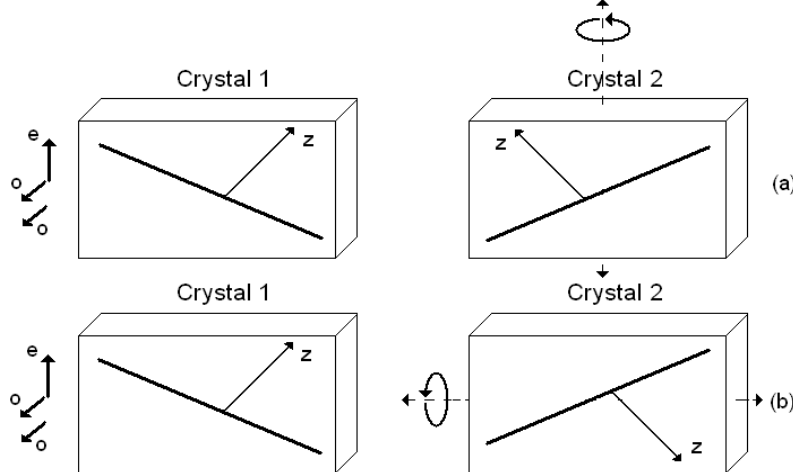


Figure 2.2 Possible orientations of the crystals for walk-off compensation. Rotation around the vertical axis (a) will preserve the effective nonlinearity (d_{eff}), whereas rotation around the propagation axis will result in opposite sign of d_{eff} in the two crystals.

Rotation around the propagation axis, shown in Figure 2.2 (b) will also result in walk-off compensation, but the inner product of the crystal z-axis and the extraordinary polarization vector changes sign, resulting in opposite sign of d_{eff} [9].

2.2.4 Acceptance angles

So far, only collinear interactions, that is, interactions of three beams with parallel wave vectors have been considered in this report. In real devices the beams have a finite divergence. Such beams consist of a superposition of plane-wave components with different directions, so it is necessary to consider interactions of non-collinear components. As explained in section 2.2.1, the phase mismatch for a fixed set of frequencies depends on the propagation direction in the nonlinear crystal. Consequently, if the crystal is oriented to give perfect phase matching for collinear beams, signal and idler components with different angles will in general have a nonzero phase mismatch. The angle interval in which the phase mismatch is small enough for efficient amplification is called the acceptance interval. If the phase mismatch varies rapidly with angle, the acceptance interval is small and only nearly collinear components will be amplified. Conversely, if the phase mismatch varies slowly with angle, the OPA can amplify even highly divergent beams.

The width of the acceptance interval depends on the birefringence of the crystal and on the polarization and propagation direction of the beams. This can be explained by use of the index ellipsoid [8]. The index ellipsoid is a three-dimensional surface that describes the refractive index of a material. For a given direction of propagation and polarization, the refractive index is found as the distance between origo and the surface along a vector that is normal to the direction of propagation and parallel to the direction of polarization.

An illustration of the index ellipsoid is shown in Figure 2.3. A plane that is normal to the propagation direction \mathbf{k} and passes through the origin of the index ellipsoid, forms an ellipse referred to as the indicatrix. The major and minor axes of the indicatrix are parallel to the displacement vectors \mathbf{D}_a and \mathbf{D}_b for the two eigenmodes. The refractive indices n_a and n_b are determined by the half-lengths of the indicatrix' major and minor axis, respectively.

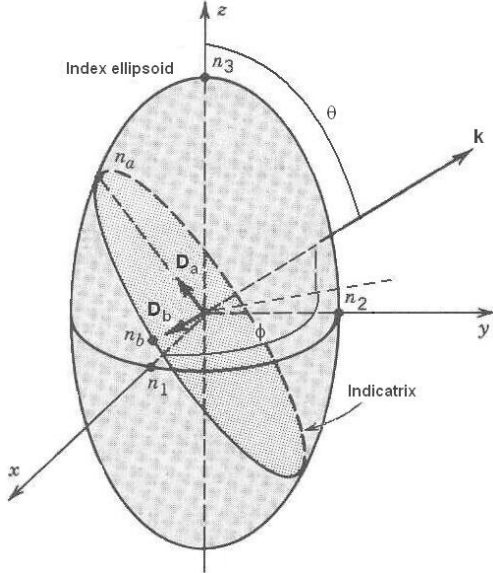


Figure 2.3 The index ellipsoid, where the coordinates (x,y,z) are the principal axes. The indicatrix is formed from the plane that is normal to the propagation direction and passes through the origin of the index ellipsoid. The refraction indices of the normal modes (n_a and n_b) are determined by the half-lengths of the axis of the indicatrix.

For a uniaxial crystal ($n_1 = n_2 = n_o$, $n_3 = n_e$, where o and e denote the ordinary and extraordinary polarization, respectively), the refractive index of one of the eigenmodes is independent of the propagation direction, i.e. n_b does not change when θ or ϕ change. The refractive index of the other eigenmode changes if the propagation direction changes in the plane of the optical axis, i.e. n_a varies when θ changes. This plane is referred to as the critical plane, and conversely, for a change in the direction normal to this plane the refractive index does not vary.

For type 2 or 3 birefringent phase-matching, where the idler and signal have different polarizations, the phase-mismatch varies if the wave changes direction in the critical plane. For changes of direction in the non-critical plane, the refractive index and hence Δk will only vary to a little extent. Therefore, the acceptance interval becomes asymmetric so that the beam can become more divergent in one direction than in the other. For type 1 birefringent phase-matching where the idler and signal have ordinary polarization, the acceptance interval becomes large. If the idler and signal both have extra-ordinary polarization, variations in refractive indices can cancel each other so that the acceptance interval becomes large even if both the refractive indices varies with the angle in the critical plane.

For a biaxial crystal ($n_1 \neq n_2 \neq n_3$) with propagation in one of the principal planes, the behavior is qualitatively the same as in the uniaxial case. One of the polarization directions is usually chosen to be parallel to a crystal axis and the corresponding refractive index is independent of the propagation direction to the first order. A propagation direction outside of the principal axes in a biaxial crystal makes the analysis more complicated, but such configurations are rarely used in nonlinear optics and will not be discussed here.

2.3 Optical parametric oscillator (OPO)

As explained in section 2.2, a nonlinear crystal driven by a pump beam can act as an optical parametric amplifier (OPA) for a signal beam. The OPO is basically an OPA placed within a resonator to provide feedback of the signal and/or idler beam(s). The OPO is singly resonant when feedback is provided for one of the beams and doubly resonant when both resonate. The parametric oscillation occurs when the gain of the OPA is greater than the roundtrip loss. Initially, only the pump is incident on the nonlinear crystal in the OPO and the signal and idler will grow from quantum noise. An important property of the parametric oscillator is that the OPA gain is not limited to certain transitions (as the laser medium gain is), leading to tunability over a wide range of wavelengths.

The OPO resonator can be realized as a linear resonator consisting of two mirrors as shown in Figure 2.4 (a), or as a ring resonator consisting of three or more mirrors, shown in Figure 2.4 (b).

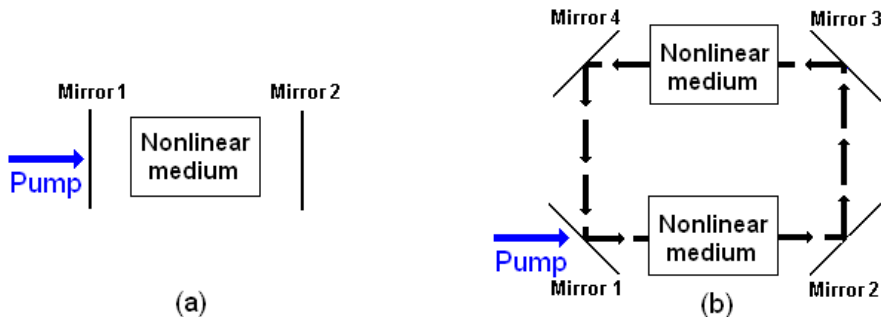


Figure 2.4 Two common realizations of the OPO resonator are shown; the linear resonator (a) and the ring resonator (b). The nonlinear medium used in this work is KTiOPO₄ (KTP) crystals.

Practical advantages of the ring resonator are prevention of pump reflection back into the pump laser and lower fluences due to only one signal propagation direction through the crystals. It is also easier to suppress non-resonant beams in the ring resonator because they can be coupled out at multiple mirrors. The drawbacks of the ring resonator are that it is more complex and more difficult to align, compared to the linear resonator [10]. Both OPO concepts have been studied in this work.

2.3.1 OPO performance parameters

The performance of an OPO can be characterized by conversion efficiency, beam quality, tuning range, power, spectral width and stability. The relative importance of the parameters depends on the application in which the OPO is being used. In this work, the most interesting

ones are those related to conversion efficiency and beam quality. The conversion efficiency of the OPO is simply the ratio between the output energy and the input energy.

The beam quality is more complicated to define. Beam quality measurements attempt to describe the complex spatial variation of the beam by one or a few numbers, so it is clear that much information is lost. The M^2 measure [11] is often used, because it has the advantage of being mathematically well behaved. M^2 is the product of the variances of the spatial fluence distributions in the near- and far field of the beam. The minimum value of this product is achieved by a Gaussian beam, and M^2 is defined to have the value 1 for such beam.

Two effects must be noted in connection with beam quality in an OPO. First, the beam quality of the signal from an OPA can be better than the beam quality of the incoming pump, as illustrated in Figure 2.5.



Figure 2.5 Evolution of the phase fronts of the beams in an OPA. The incoming phase front of the pump (blue) is poor, whereas the the phase front of the signal (green) is good. The phase front of the pump can be transferred to the idler (red), not affecting the phase front of the signal. In this way, the beam quality of the amplified signal can become better than that of the pump.

The poor phase front of the pump can be transferred to the idler and does not affect the phase front of the signal. More important is that this mechanism allows a singly resonant OPO to produce a signal with better beam quality than that of the pump.

Second, the pump beam forms a transverse gain profile in the nonlinear medium. This leads to reshaping of the signal beam and preferential amplification of components with small divergence, so-called gain guiding, which can improve the beam quality.

2.3.2 Power scaling

In order to scale an OPO from low to high energies the beam diameter has to be increased to keep the energy concentration (fluence) below the damage threshold. The result of increasing the beam diameter is a high-Fresnel-number cavity ($N_F = d^2/\lambda L$, where N_F is the Fresnel-number, d is the beam diameter, λ is the wavelength and L is the cavity length) where the gain guiding is not sufficient to suppress higher-order transverse modes. Efficient conversion of high energy beams in OPOs using traditional flat mirror resonators generally result in highly divergent beams (low beam quality), due to poor transverse mode control over the generated beam [12]. Fortunately, there are several methods that can be used in order to improve beam quality in high N_F OPOs, for example image flipping/rotation [12] or two-stage systems. In a previous work, the latter was identified as most promising for this application [13].

2.3.3 Master oscillator/power amplifier

An approach to scale up the energy without compromising the beam quality is to use a two-stage system consisting of a master oscillator (OPO) and a power amplifier (OPA), referred to as a master oscillator/power amplifier (MOPA). Figure 2.6 shows the two stages of a MOPA system. The basic idea behind the configuration is to pump the OPO with a beam with small diameter, which produces a low-energy OPO signal with high beam quality. A high-energy pumped OPA is then used to amplify the low-energy signal coming out from the OPO, giving a high-energy OPA signal of high beam quality [14].

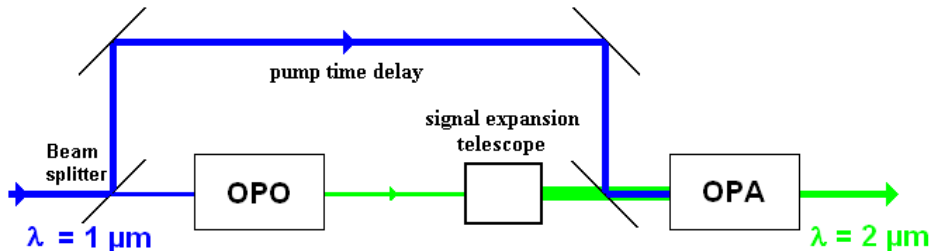


Figure 2.6 A two-stage master oscillator/power amplifier (MOPA) configuration. The OPO is pumped with a narrow beam and produces a narrow signal with relatively high beam quality. The signal is used as seed for the OPA and expanded to fill the transverse area of the OPA crystals. The OPA is pumped with a wide beam of high energy. The OPA pump must be properly delayed relative to the OPO signal so that their pulses are synchronized.

For maximum gain and efficiency, the pump time delay must be chosen so that the OPA pump pulse is synchronized with the OPO signal pulse. The problem can be illustrated in Figure 2.7. The OPO signal pulse is delayed about 3 nanoseconds relative to the OPO pump pulse, due to the build-up time of the OPO. Since the same pump is used to pump both the OPO and the OPA, the OPA pump has to be propagated through an external path with a certain length that eliminate the time delay between the pulses at the power amplifier.

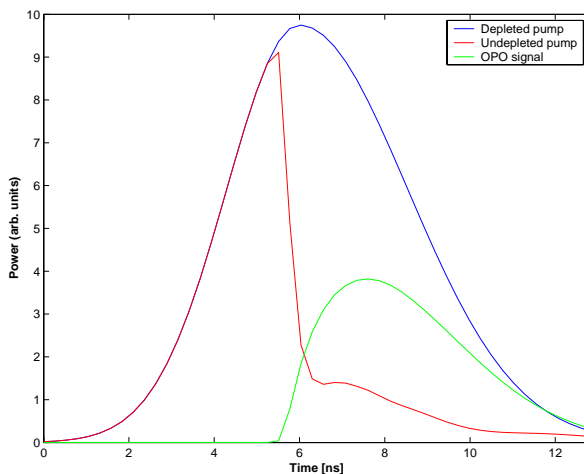


Figure 2.7 Time evolution of the pump and signal power in an OPO. The signal pulse is delayed about 3 ns relative to the pump pulse due to the build-up time of the resonator.

The transversal interaction region between the two beams in the OPA crystals is confined to the diameter of the narrowest beam. If the signal beam diameter is too small, only a part in the middle of the pump will be depleted, leading to low conversion efficiency. Thus, in the experiments, the OPO signal is expanded so that as much as possible of the uniform part of the fluence distribution covers the OPA crystals. This expansion of the OPO signal results in spatial filtering of the beam. Only the middle part of the beam is used and the most divergent angle components are not passed on to the OPA stage. Thus, the beam quality of the signal beam to be amplified in the OPA can be better than that coming out of the OPO.

2.4 Pump characteristics

The performance of the OPO and OPA depends on the characteristics of the laser beam used as the pump. Some fundamental aspects of the pump are presented in the following.

2.4.1 The pulse

The lasers used to pump OPOs can be categorized according to the duration of the pulses they produce, e.g. continuous wave (CW), Quasi CW, Q-switched and mode-locked lasers. The pulse duration influences the design of the OPO resonator. Q-switched type lasers, such as the one used in this assignment, typically produce nanosecond pulses. The distribution of the pump power during the pulse (the pulse shape) and the pump energy have major impact on the conversion efficiency of the OPO.

The build-up time of the OPO is critical for efficient operation, since the pump energy that is sent through the resonator before the signals have grown strong enough to deplete the pump is wasted. The build-up time is generally given by the roundtrip gain of the OPO and the roundtrip time. The higher the pump power is above the threshold, the shorter the build-up time becomes, because the initial gain in the OPO is increased. This is illustrated in Figure 2.8 (a) and (b).

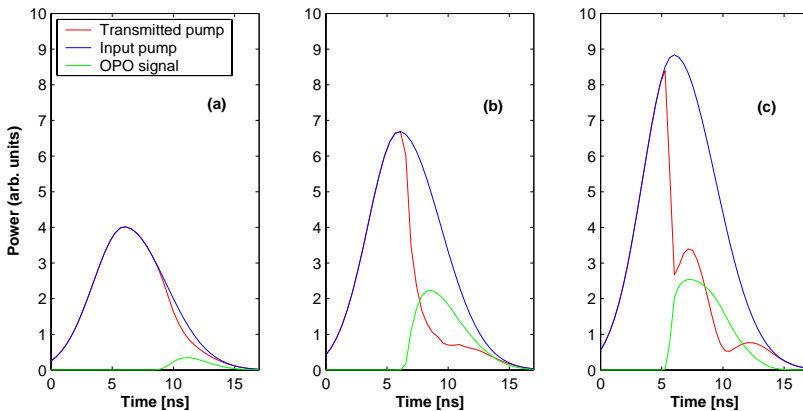


Figure 2.8 Time evolutions of the power in an OPO pumped with different energy. The input pump energy is just above threshold (a), the input pump energy is suited to obtain short OPO build-up time at the same time as back-conversion is prevented (b), and the input pump energy is too high, resulting in back-conversion (c).

Short OPO resonators have faster build-up time because the number of roundtrips the beam makes during the pulse is increased. However, there is a trade-off between conversion efficiency and back-conversion. Too high pump power result in back-conversion when the signal reaches maximum power and in the later stages of the pump pulse, as illustrated in Figure 2.8 (c).

Generally, there is a greater risk for back-conversion when short pulses are used to pump the OPO, because high gain is required to provide for fast build-up time of the signal. Also, it is more difficult to obtain a signal with high beam quality for short pulses in an OPO, because the number of roundtrips, in which the most divergent angle-components of the signal is being spatially filtered, is decreased.

2.4.2 The intensity distribution

The intensity distribution of the pump determines the spatial distribution of gain in the nonlinear crystal. In order to obtain efficient conversion, the beams used to pump the OPO and OPA should have a close to uniform intensity distribution. If the fluence is unevenly distributed, the different parts of the signal beam will have unequal gain and will be depleted at different rates, leading to inefficient conversion and problem with back-conversion.

A Gaussian beam has a transverse distribution that is not uniform. Thus, a Gaussian beam is not necessary optimal for pumping a nonlinear crystal, even though it has the best possible beam quality in terms of M^2 . Many high-energy lasers produce transverse distributions that are more flat-topped than Gaussian, because the aperture of the laser rod clips the beam. However, it must be noted that even if the fluence distribution (J/cm^2) is approximately uniform, the intensity distribution (W/cm^2) can vary during the pulse [15].

Another problem is that most laser beams change their transverse profile under propagation, so a uniform distribution at the laser output can be deteriorated when it reaches the frequency conversion device. This is particularly relevant for the MOPA, where the pump path to the OPA must be relatively long. However, implementation of lens systems in the propagation path can reduce the deterioration of the fluence distribution. A possible solution, which both transfers the intensity distribution from the laser to the OPA and allows the beam diameter to be scaled to the desired size, is the relay-imaging telescope, shown in Figure 2.9.

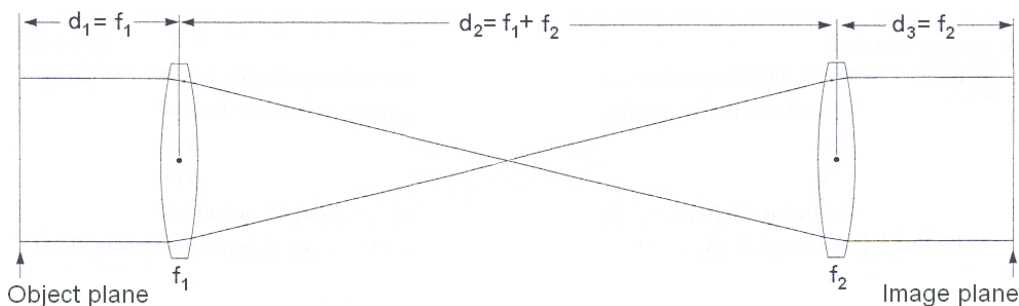


Figure 2.9 The relay-imaging telescope. Both the intensity distribution and the wavefront of the beam at the object plane is recreated at the image plane.

In this lens-system the fluence distribution at the object plane is transferred and recreated in a scaled version at the image plane. Its operation can be explained by the ABCD-matrix [16]

$$M_{RIT} = \begin{bmatrix} -\frac{f_2}{f_1} & 0 \\ 0 & -\frac{f_1}{f_2} \end{bmatrix}, \quad (2.11)$$

which shows that the beam diameter is scaled by a factor f_2/f_1 and the divergence is reduced by the inverse factor. A lens system consisting of one convex lens for normal imaging is not suitable for this application, because it images only the intensity and not the wavefront. On the contrary, the relay-imaging telescope reproduces both the intensity and the wavefront of the pump beam.

A disadvantage of the relay-imaging telescope is an unavoidable intermediate focus that brings along the risk of break down and difficulties in folding the path. An imperfect alternative without the focus is shown in Figure 2.10.

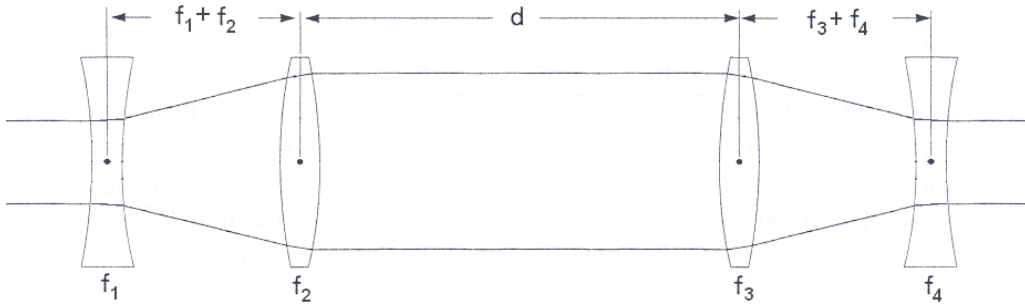


Figure 2.10 Lens telescopes that expand and decrease the beam diameter in order to reduce the effective propagation length.

The principle of operation is that diffraction is reduced in the expanded part of the beam, and this reduces the effective propagation length as far as change of transverse distribution is concerned. However, the ABCD-matrix of the lens system

$$M_T = \begin{bmatrix} \frac{f_2 f_4}{f_1 f_3} & -\left(\frac{f_1 f_3}{f_2} + \frac{f_2 f_4}{f_3}\right) \\ 0 & \frac{f_1 f_3}{f_2 f_4} \end{bmatrix} \quad (2.12)$$

lacks the simple diagonal form of (2.11), so it does not reproduce an exactly scaled version of the input beam. Both lens systems were tried in the experiments.

2.4.3 Beam quality

As mentioned in section 2.3.1, the beam quality describes the divergence properties of the beam. A pump of low divergence (high beam quality) is important in order to achieve efficient

conversion in OPOs where acceptance intervals are small. Highly divergent components of the pump will not contribute to the gain in the nonlinear medium, due to non-perfect phase-matching (see section 2.2.4).

The divergence of the pump also determines the rate at which the transverse distribution deteriorates under propagation. The better the beam quality of the pump is, the less the deterioration becomes. Deterioration can result in local spikes in the transverse distribution of the beam, which leads to non-uniform spatial distribution of the gain in the nonlinear medium.

3 EXPERIMENTS

The pump laser used in the experiments was a Quantel Brilliant B flashlamp pumped Nd:YAG (Neodymium doped Yttrium Aluminum garnet) laser and it delivered 1.064 μm pulses of 800 mJ at 10 Hz repetition rate, while the pulse length was about 6 ns (FWHM). The laser operated on multiple longitudinal modes with a spectral width of approximately 20 GHz [17] and the beam quality was measured to be $M^2 \approx 2$. The beam diameter was approximately 8 mm at the laser output aperture.

Because of thermally induced strain in the laser rod, about 15 % of the output energy from the laser had vertical polarization. The first polarizer (P_1) in all of the experimental setups removed this unwanted polarization and made the transmitted beam horizontally polarized. The energy in the laser beam was measured to be 780 mJ and 660 mJ before and after the first polarizer, respectively.

KTiOPO₄ (KTP) crystals were chosen as the nonlinear material because they have high damage threshold and fairly high nonlinearity. The propagation direction in the KTP crystals was chosen to be $\theta = 50.5^\circ$ and $\phi = 0^\circ$, i.e. propagation in the xz-plane. The birefringent phase-matching was of type 2 (oeo), giving the pump and idler the fast polarization and the signal the slow polarization. The theoretical signal and idler wavelengths for this propagation direction was 2.090 μm and 2167 μm , respectively, based on Sellmeier equations [18]. The relevant nonlinear tensor element for this interaction was $\chi_{yyz} = 2d_{yyz}$, where $d_{yyz} \approx 2.5 \text{ pm/V}$ [19]. The walk-off angle of the signal beam was 47 mrad. Typically, uncoated KTP crystals have a 1.064 μm damage threshold well above 10 J/cm² [20, 21]. However, the KTP crystals used in the lab had AR-coatings with considerably lower damage threshold, and the supplier recommended limiting the fluence to $\sim 3 \text{ J/cm}^2$.

3.1 Preliminary experiment

The first OPO pump path that was tested in the laboratory is shown in Figure 3.1. This configuration was implemented in the project assignment.

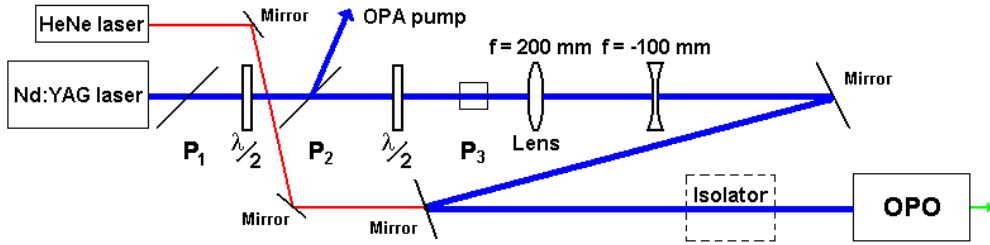


Figure 3.1 The first experimental OPO configuration. The distance from the Nd:YAG laser to the first lens was 57 cm. A distance of 12 cm separated the two lenses, and the distance from the last lens to the OPO was approximately 170 cm, giving a total OPO pump path length of 239 cm. With this lens configuration the OPO was pumped with the far field of the laser beam.

The polarizers (P_2 and P_3) together with the half-wave retarders ($\lambda/2$) formed two variable attenuators that made it possible to easily adjust both the amount of energy that pumped the OPO and the energy split off to the OPA. The two lenses were positioned so that the beam had a diameter of about 1 mm over the length 15 cm where the OPO was placed. Also, the lens configuration resulted in the OPO being pumped with the far field of the laser beam. In this context, the term far field denotes a fluence distribution that corresponds to the far field of the raw laser beam. The far field fluence distribution of the Nd:YAG laser beam used to pump the OPO in the preliminary experiment is shown in Figure 3.2. The picture was taken with a CCD camera connected to a computer with a frame-grabber.

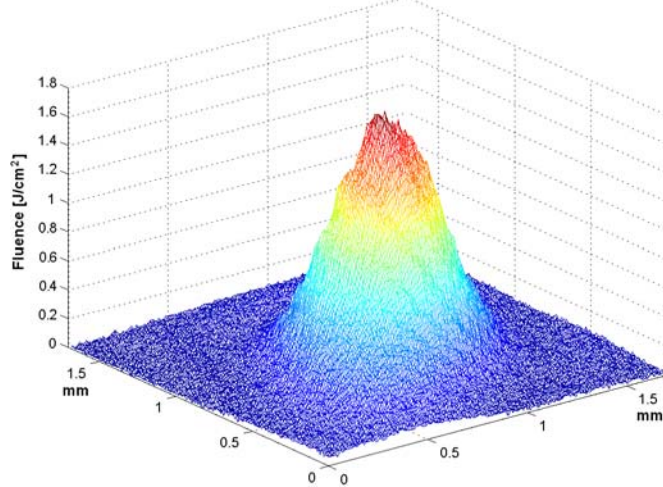


Figure 3.2 The far field fluence distribution of the OPO pump in the preliminary experiment. The pump energy was 8 mJ and the beam diameter for 90 % encircled energy was approximately 1 mm at the OPO.

3.1.1 Ring OPO

The ring OPO implemented in the lab is shown in Figure 3.3. This implementation was based on simulations in the project assignment. In the resonator, the idler was completely transmitted through all of the mirrors, whereas the signal was partially (~30 %) transmitted through mirror 2, referred to as the output coupling mirror. The pump was completely transmitted at mirrors 1 and 4, and totally reflected at mirrors 2 and 3.

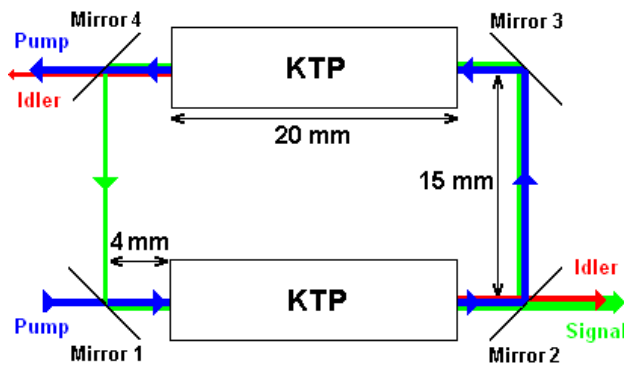


Figure 3.3 The ring OPO with 20 mm KTP crystals. The signal was partially coupled out at mirror 2. The total air gaps between the crystals were 23 mm at each side. The pump was reflected at mirror 2 and 3, and transmitted at mirror 4. The idler was transmitted at all mirrors.

To achieve parametric oscillation at the desired wavelengths (signal at 2090 nm and idler at 2167 nm), the crystals were tuned (in a temporary linear resonator) to the correct angle using a spectrometer to measure the wavelength. Then, the mirrors in the ring resonator were positioned and adjusted in a specific order. Overlapping a HeNe laser beam with the Nd:YAG laser beam, shown in Figure 3.1, made it possible to align these mirrors using the visible ($\lambda = 632.8$ nm) and low-intensity HeNe beam.

First, mirror 1 was placed in the pump path a few centimeters before its intended position in the resonator. This made it possible to align the three other mirrors at the same time as the deflection from mirror 1 was taken into consideration. Mirror 2 was positioned and adjusted so that it reflected the laser beam horizontally at an angle of 90 degrees towards mirror 3. The same procedure was carried out for the last two mirrors. Finally, mirror 1 was moved into the correct position and adjusted so that the incoming beam and the beam that had traveled one roundtrip in the resonator coincided. Actually, careful alignment of the resonator mirrors with the HeNe beam resulted in oscillation once the pump beam was turned on. Further fine adjustments of the mirrors (mainly mirror 1 and 4) and the angle of the second crystal maximized the output energy.

Unfortunately, the experiment revealed that the available output coupling mirrors were damaged at only 8 mJ pump energy. Therefore, the ring OPO could only be operated safely at pump energies up to 7 mJ. This was a temporary setback, since the computer simulations in the project assignment had showed that the optimal operation point for the ring OPO was at approximately 11 mJ pump energy.

Furthermore, the optimized ring OPO pumped at 7 mJ pump energy and with 20 % output coupling produced no more than 6 % efficiency (signal) and had a relatively high threshold of 3.8 mJ. This performance was much poorer than predicted by computer simulations, where 16 % conversion efficiency had been obtained. The reasons for this deviation are probably time variation of the pump beam profile during the pulse, and difficulties in adjusting the ring OPO optimally.

Pictures were taken of the signal and idler using a pyro-electric camera and it could be seen that the signal was asymmetric and had a poor fluence distribution. To avoid the vulnerable mirrors and to simplify alignment, we resorted to a linear resonator.

3.1.2 Linear OPO

The mirrors of the linear OPO, shown in Figure 3.4, were designed for singly resonant operation and 2-pass pump, i.e. mirror 1 reflected the signal and transmitted the pump and idler, while mirror 2 reflected the pump, transmitted the idler and partially transmitted the signal.

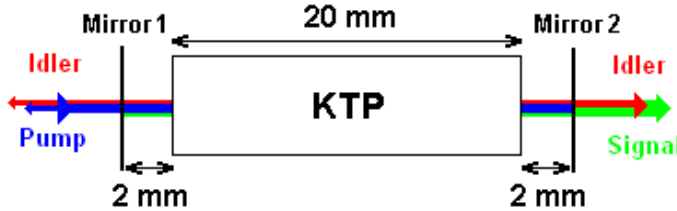


Figure 3.4 The linear OPO. The 20 mm KTP crystal and the mirrors were separated by 2 mm air gaps. The pump was reflected at mirror 2 and the idler was transmitted at both mirrors.

The dynamics of the implemented linear OPO were approximately identical to that of the ring OPO. Both had double pass geometry for the pump and signal, whereas the idler was coupled out at the mirrors. The differences were somewhat higher fluence in the crystal and smaller air gaps in the linear OPO. The idler was not completely coupled out at the mirrors, resulting in the linear OPO not being perfectly singly resonant.

A Faraday isolator was placed in front of the OPO (see Figure 3.1) to prevent reflection of the pump back into the pump laser. The energy loss in the isolator was measured to be about 12 %. The KTP crystal in the OPO was tuned so that the signal and idler wavelengths were $2.080 \mu\text{m}$ and $2.173 \mu\text{m}$, respectively. The reason for this was to exploit the frequency response of the OPO mirrors for best possible singly resonant operation. With 2 mm long air gaps between the crystals and the mirrors, the linear OPO had a threshold at 2.3 mJ pump energy and a conversion efficiency of about 16 % at 8 mJ, which is a significant improvement compared to the ring OPO (just 6 % at 7 mJ). The explanations for this improvement can be that the linear OPO was easier to adjust. It also had shorter air gaps, fewer mirrors (less loss) and was slightly doubly resonant. Pictures taken of the signal beam showed improved appearance compared to the ring OPO and is shown in Figure 3.5.

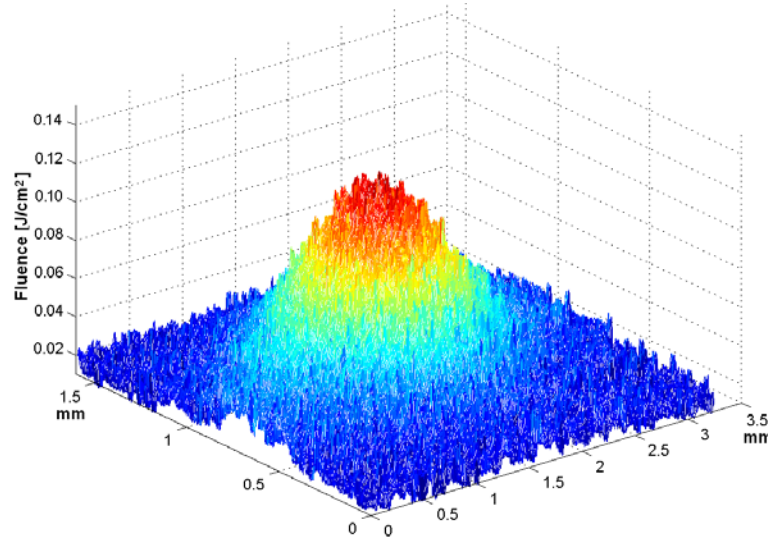


Figure 3.5 The fluence distribution of the signal of the linear OPO pumped with the far field of the laser beam.

3.1.3 OPA pump paths

In designing the path of the OPA pump beam, both a proper OPA pump beam diameter and an appropriate time delay between the OPO signal pulse and the OPA pump pulse had to be taken into consideration. The length of the OPO path was 271 cm (laser to OPO plus OPO to OPA) and, from simulations, the optimal time delay was 2.6 ns (78 cm). This resulted in the OPA pump path length being approximately 350 cm.

In a preliminary experiment, two $4 \times 4 \text{ mm}^2$ KTP crystals were used in the OPA. Thus, the total crystal length was 30 mm and was chosen on basis of the optimal crystal length in simulations with single-longitudinal mode pump (see Figure 4.4). The two crystals were orientated for walk-off compensation of the signal, as shown in Figure 3.6.

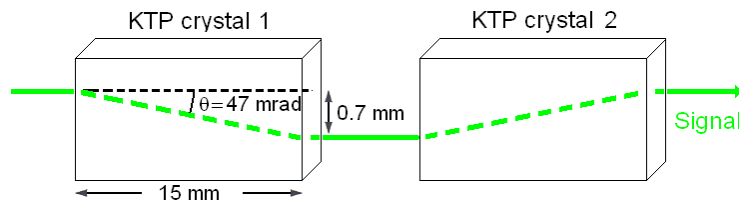


Figure 3.6 Signal walk-off in the OPA crystals. The walk-off angle in the KTP crystal was 47 mrad, causing the signal to drift a transversal distance of 0.7 mm in the 15 mm long crystals. Correct orientation of the second crystal eliminated transversal displacement of the outgoing signal relative to the incoming.

Measurements performed showed that the conversion efficiency of the MOPA was almost halved when the last crystal was incorrectly orientated, compared to when it was correctly orientated, as discussed in section 2.2.3.

A common way to adjust the pump time delay is to include an adjustable prism reflector in the OPA pump path. However, careful characterization of the pump beam revealed that the spatial

distribution deteriorated a few decimeters after the output aperture of the laser. Figure 3.7 shows the fluence distribution of the Nd:YAG laser beam after 2 meters of propagation in air.

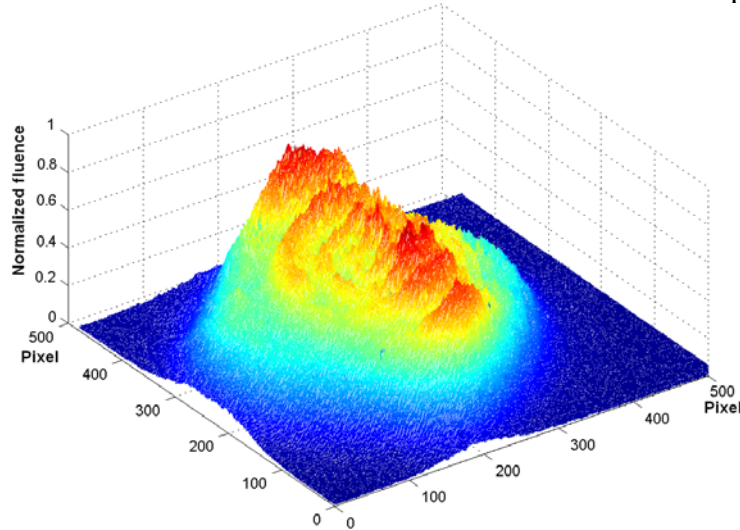


Figure 3.7 The fluence distribution of Nd:YAG laser having propagated 2 meters in air. The fluence distribution was not suited for pumping the OPA.

3.1.3.1 Relay-imaging telescope

A favorable pump beam, with a relatively flat top, could be obtained by imaging from a point about 10 cm or more behind the output aperture of the laser. For this purpose the relay-imaging telescope shown in Figure 3.8 was implemented. Combining relay-imaging with an adjustable length is complicated, so we designed the OPA pump path to have a fixed length.

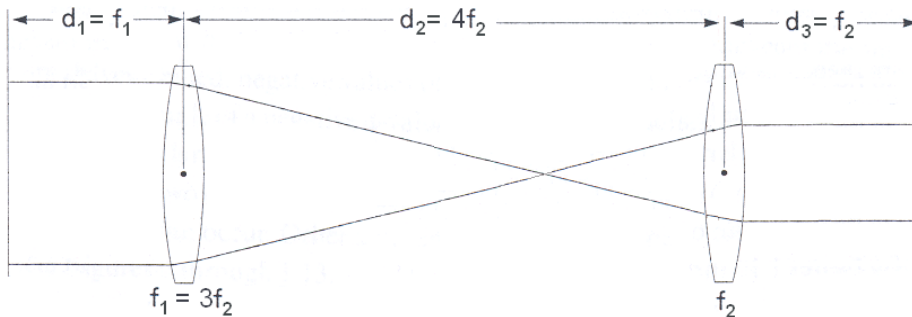


Figure 3.8 The relay-imaging telescope in the OPA pump propagation path used to image the Nd:YAG laser beam. The beam diameter was reduced by a factor 3 at the OPA crystals.

With $f_2 = 500$ mm the length of the OPA pump path became 4 meters. The implemented MOPA-configuration is shown in Figure 3.9.

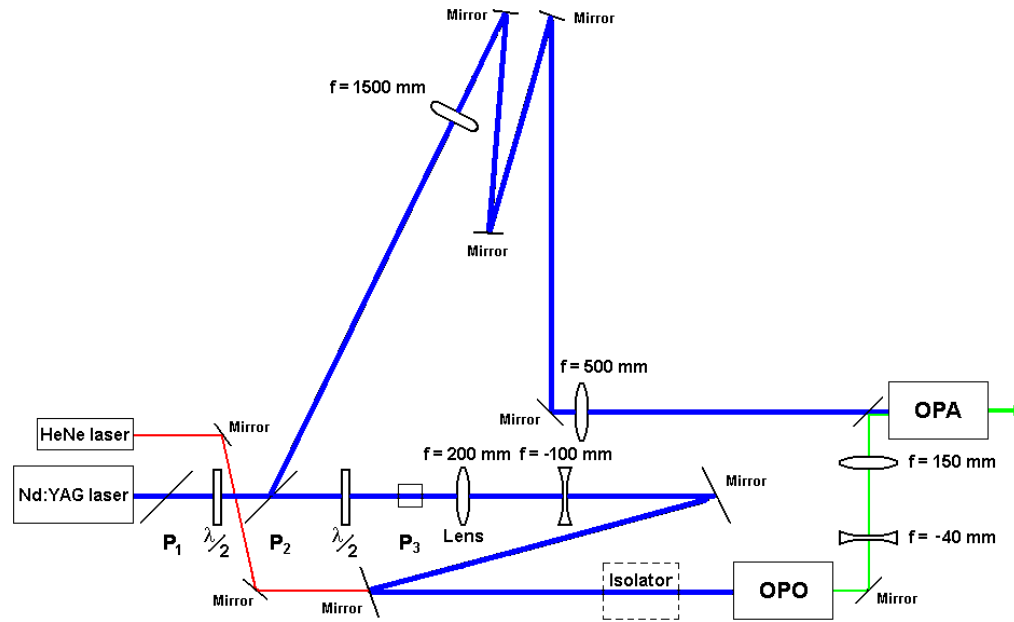


Figure 3.9 The implemented MOPA configuration with two $4 \times 4 \text{ mm}^2$ OPA crystals. The OPA pump diameter was approximately 2.6 mm at the crystals and the OPO signal was expanded by a factor 3.75.

The OPO signal beam was expanded in a telescope ($f = -40 \text{ mm}$ and $f = 150 \text{ mm}$ lenses in Figure 3.9) by a factor 3.75 to entirely cover the $4 \times 4 \text{ mm}^2$ KTP crystals. The diameter of the OPA pump at the OPA crystals was estimated, on basis of 90 % encircled energy, to be 2.6 and 2.5 mm in the horizontal and vertical directions, respectively. The relay-imaging telescope resulted in the object plane being approximately 50 cm behind the output aperture of the laser. This gave an acceptable fluence distribution at the OPA crystals, as shown in Figure 3.10.

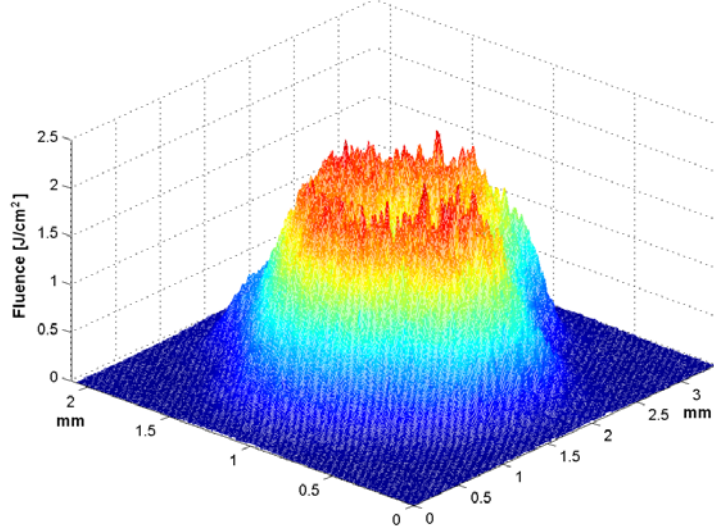


Figure 3.10 The fluence distribution of the relay-imaged OPA pump. The object plane was 50 cm behind the output aperture of the laser and the diameters were 2.6 and 2.5 mm in the horizontal and vertical directions, respectively.

With 70 mJ pump energy and two 15 mm long crystals the conversion efficiency of the MOPA was measured to be approximately 40 % (idler and signal). Estimations indicated that the OPA could be operated safely (below fluence damage threshold) at 90 mJ pump energy, but due to

unwanted breakdown in the air at the focal point of the first lens of the relay-imaging telescope, higher pump energies could not be used.

3.1.3.2 Expansion telescopes

The intermediate focus is an unavoidable feature of the relay-imaging telescope. Therefore, an attempt to operate the OPA at higher pump energies was made by implementing a non-imaging propagation system that reduced the effective propagation length by beam expansion. The lens system is shown Figure 3.11.

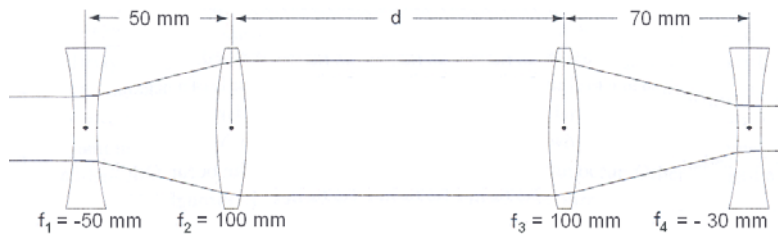


Figure 3.11 The lens system for expansion of the OPA pump. The first telescope ($f_1 = -50 \text{ mm}$ and $f_2 = 100 \text{ mm}$) doubled the pump beam diameter, whereas the second telescope ($f_3 = 100 \text{ mm}$ and $f_4 = -30 \text{ mm}$) reduced the beam diameter to about one third.

The laser beam was expanded in a telescope placed in the OPA pump path shortly after the second polarizer (P_2) and narrowed down to wanted size in a second telescope placed just before the OPA crystals. The fluence distribution of the beam having propagated 2 meters is shown in Figure 3.12 and it was clearly deteriorated compared to the flat-topped fluence distribution of the relay-imaging telescope (Figure 3.8).

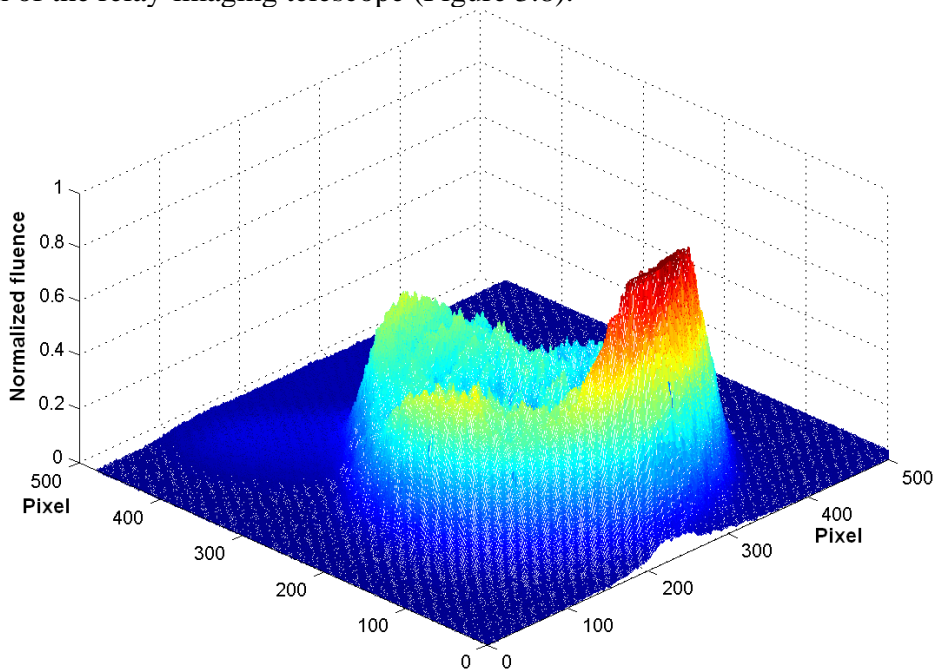


Figure 3.12 The fluence distribution of the OPA pump having propagated 2 meters in the expansion lens system. The fluence distribution was deteriorated compared to that of the relay-imaging telescope.

Thus, the relay-imaging telescope was the preferred solution for the high-energy scaled OPA, assuming that the problem with breakdown in the intermediate focus could be solved.

3.1.4 OPO pump pulse characterization

In order to investigate why the OPO efficiencies for both the linear and ring resonator were poor, a more accurate characterization of the OPO pump beam was carried out in the lab.

One hypothesis was that the shape of the pump beam varied through the pulse. To inspect this, the OPO was removed and a 50 mm lens was placed in the OPO pump 60 mm after the OPO center position to enlarge the beam. Then, an aperture was placed 300 mm after the lens. The aperture was moved to direct different parts of the beam onto a silicon photo diode detector. Thus, by connecting an oscilloscope to the detector it was possible to investigate the variation of the pulse shape with transversal position. Figure 3.13 shows the pulse shapes of the OPO pump beam at 7 different positions.

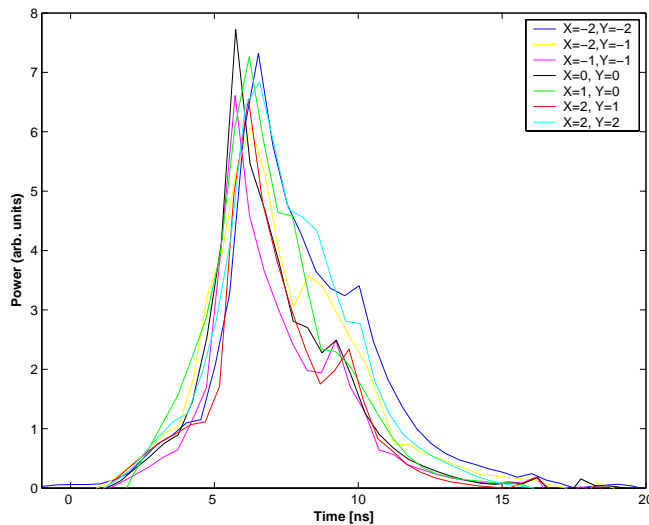


Figure 3.13 Pulse shapes of seven different transversal positions of the OPO pump. The legend gives x- and y-coordinate position of the aperture, where $X = 0$, $Y = 0$ was in the center of the beam. The curves indicate shorter pulses in the center of the pump beam than in the outer parts.

Both the pulse shape and the pulse length fluctuated significantly from pulse to pulse, so the characterization was not very precise. However, there is a clear tendency in Figure 3.13 that the pulses are longer further from the beam center, and this may well have reduced the performance of the OPO.

3.1.5 Relay-imaging telescope in the OPO pump path

Although the results of the pump beam characterization were not quite clear, we decided to try the linear OPO with a relay-imaged pump beam. The implemented OPO pump path configuration is shown in Figure 3.14.

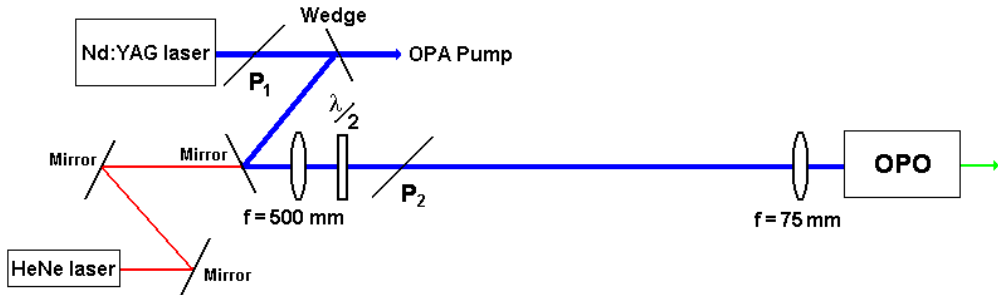


Figure 3.14 The relay-imaging telescope in the OPO pump path, where $f_1 = 500\text{mm}$ and $f_2 = 75 \text{ mm}$, giving a magnification factor of 0.15. The distance from the laser output aperture to the first lens was 31.5 cm and the distance between the lenses was 60.5 cm. The object plane was 18.5 cm behind the output aperture of the laser (i.e. inside the laser) and the OPO pump path length was 112 cm. The energy split off from the wedge used to pump the OPO was approximately 21 mJ. The wave retarder and the polarizer (P_2) formed a variable attenuator that made it possible to control the energy in the OPO pump.

There was no need for an isolator in this implementation, because the amount of energy passed back into the pump laser when the reflected pump hit the wedge was insignificant. With the two chosen relay-imaging telescope lenses given in Figure 3.14 the magnification of the beam was $m = 0.15$, the object plane was 18.5 cm behind the output aperture of the laser (i.e. inside the laser) and the OPO pump path length was 112 cm. Thus, this configuration had roughly a meter shorter pump path length compared to the first OPO setup. The fluence distribution of the OPO pump with this configuration is shown in Figure 3.15.

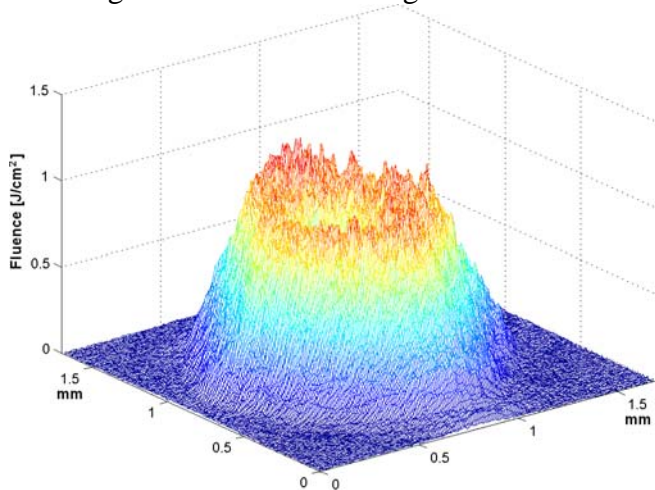


Figure 3.15 The fluence distribution of the relay-imaged OPO pump. The object plane was 18.5 cm behind the laser output aperture and the beam diameter was approximately 1.2 mm.

Pumped with the relay-imaged fluence distribution, the linear OPO had a conversion efficiency of 22 % (signal) at 8 mJ pump energy, whereas the corresponding efficiency was 16 % when pumped with the far field fluence distribution. Figure 3.16 shows the measured I/O curves for the linear OPO pumped with the far field and relay-imaged fluence distributions.

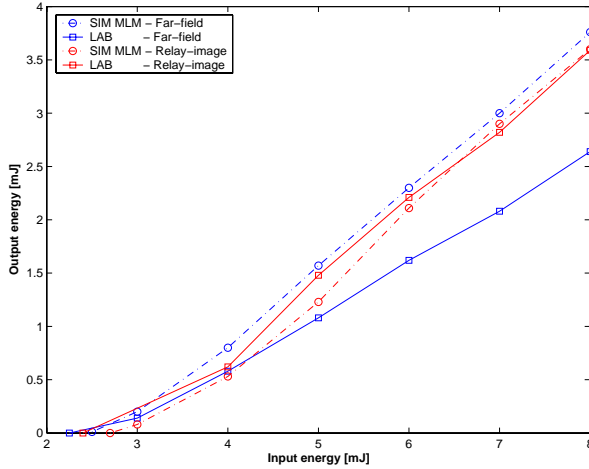


Figure 3.16 Measured and simulated I/O curves for the linear OPO pumped with the far field and the relay-imaged fluence distribution.

The reasons that the measured conversion efficiency of the far field pump was lower than that of the relay-imaged pump are probably related to the time variation of the far field pump beam. These variations were not included in the simulations and may have caused the large deviation between the simulated and measured values for the far field pump, as shown in the Figure 3.16.

The fluence distribution of the output signal of the linear OPO with the relay-imaging telescope in the OPO pump path is shown in Figure 3.17.

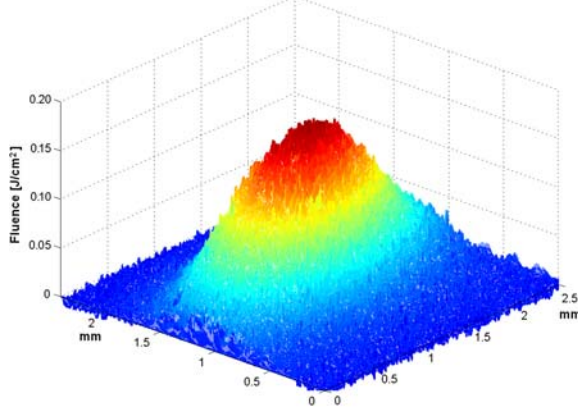


Figure 3.17 The fluence distribution of the signal of the linear OPO pumped with the relay-imaged fluence distribution.

For signal beam characterization we formed a waist with an $f = 200$ mm lens and obtained the corresponding far field with a second $f = 250$ mm lens. The beam widths were measured independently with a scanning knife-edge and the M^2 beam quality was estimated from the 16-84 % knife-edge widths with the method from Ref. [22]. Table 3.1 shows the beam parameters for the OPO. The waist diameters, d_x and d_y , are defined to be two times the 16-84 % knife-edge width, so that they equal the $\exp(-2)$ diameter for a Gaussian beam. The divergence angles, θ_x and θ_y , are defined analogously, so the product $d \times \theta$ would be $4\lambda/\pi = 2.65\text{mm} \times \text{mrad}$ for a Gaussian beam with $\lambda = 2.08 \mu\text{m}$. We emphasize that only the product $d \times$

θ represent real measurements, the M^2 values are estimates that are not based on the true second moments. Also note that the estimation of M^2 from the product $d \times \theta$ includes a correction factor; it is not simply a division by the value for a Gaussian beam [22].

	$d_x \times \theta_x$	$d_y \times \theta_y$	M_x^2	M_y^2	M^2
OPO	4.75	11.1	1.6	3.4	2.6

Table 3.1 Signal beam parameters for the OPO. The widths d and θ are two times the 16%–84% knife-edge width, and the x and y coordinates correspond to the critical and noncritical directions, respectively. M^2 is an estimate of the overall beam quality, based on the RMS values of the x and y widths.

3.2 The MOPA configuration scaled to higher energy

The next part of the implementation in the lab involved construction of a MOPA configuration that made it possible to utilize the maximum available energy from the Nd:YAG laser. This meant replacing the $4 \times 4 \text{ mm}^2$ diameter crystals in the OPA with larger $8 \times 8 \text{ mm}^2$ KTP crystals and constructing a new relay-imaging telescope (including a vacuum tube) in the OPA pump path.

3.2.1 OPA pump energies up to 400 mJ

KTP crystals with diameters of $8 \times 8 \text{ mm}^2$ were implemented in the OPA and thus the magnification of the laser beam had to be just slightly below 1. Using the two lenses $f_1 = 750 \text{ mm}$ and $f_2 = 500 \text{ mm}$ in the OPA pump path shown in Figure 3.18 gave a magnification of $m = 0.67$. The resulting beam was slightly elliptic and had beam diameters of approximately 5.8 mm and 4.4 mm in the horizontal and vertical direction, respectively, at the OPA crystals. The length of the OPA pump path became 215 cm, which was about half the length of the previous MOPA configuration (400 cm).

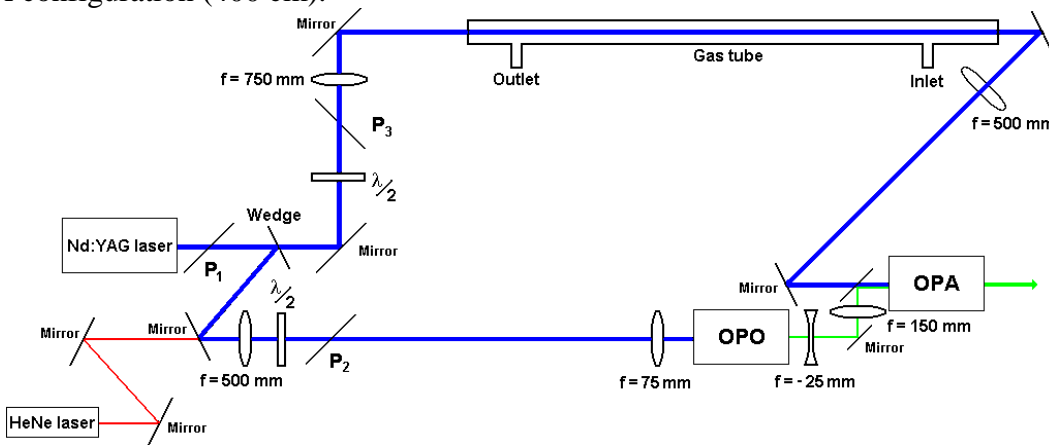


Figure 3.18 The MOPA configuration for OPA pump energies up to 400 mJ. The lenses ($f_1 = 750 \text{ mm}$ and $f_2 = 500 \text{ mm}$) of the relay-imaging telescope in the OPA pump path gave a 90 % encircled energy beam diameter of approximately 5.8 and 4.4 mm in the horizontal and vertical direction, respectively, at the OPA crystals. The OPA pump path length then became 215 cm. The OPO signal was expanded by a factor 6.

An evacuated glass tube with Brewster windows was placed into the OPA pump path to cover the area around the intermediate focus of the relay-imaging telescope. This prevented breakdown, even for maximum OPA pump energy (~ 600 mJ). The OPO signal was expanded by a factor 6 in a telescope consisting of a concave $f = -25$ mm lens and a convex $f = 150$ mm lens to cover the OPA crystal entirely. The OPO signal and OPA pump were made collinear by using the pyro-electrical camera. The folding mirrors were adjusted so that the transversal distribution of the two beams overlapped at the OPA and at a point approximately 1 meter behind the OPA.

The measured and simulated I/O curve for this MOPA configuration is shown in Figure 3.19.

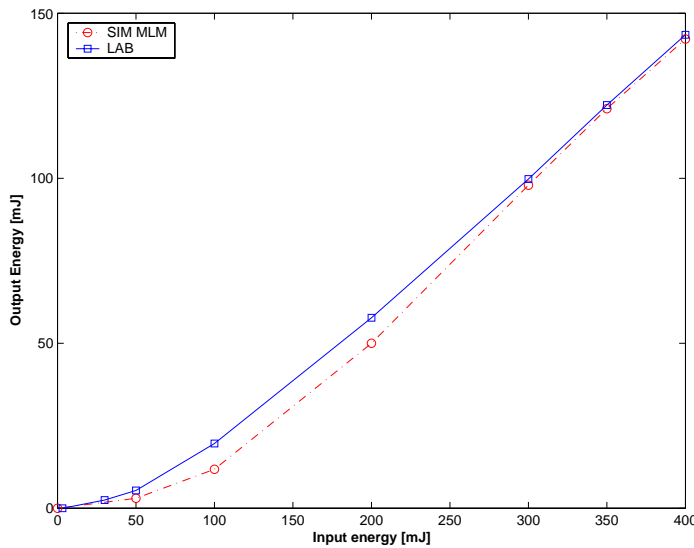


Figure 3.19 Measured and simulated I/O curve for the MOPA with 5.8×4.4 mm 2 OPA pump beam diameter and 6 times expansion of the signal beam.

The output energies were measured with an energy meter placed after a filter that separated the pump beam from the signal and idler beams. Characterization of the filter showed that about 80 % of the signal and 98 % of the idler was transmitted through the filter. Thus, the energies in Figure 3.19 are the measured energies multiplied by a factor 1.12 (when equal amount of energy in signal and idler is assumed) to adjust for the losses in the filter. The pump fluence at the OPA crystals was approximately 3.3 J/cm 2 at 400 mJ. At this pump energy the conversion efficiency of the MOPA was 36 % (signal and idler).

In order to investigate the timing between the OPA pump and the OPO signal at the OPA crystals and the depletion of the pump in the OPA, measurements of the pulse shapes were carried out. These measurements are shown in Figure 3.20.

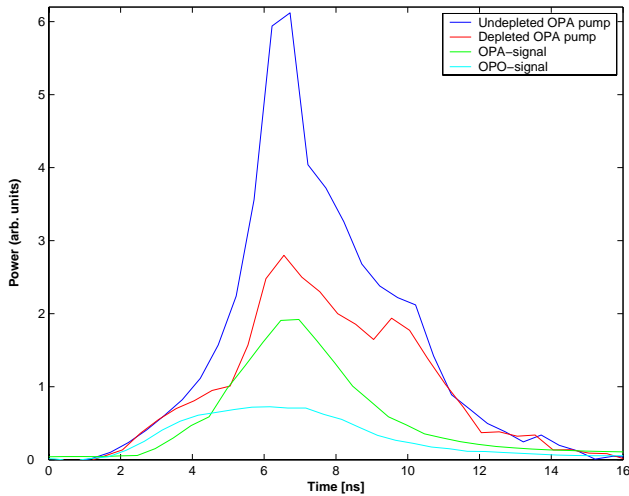


Figure 3.20 *Measured time evolution of the beams in the OPA pumped with 300 mJ. The graphs show relatively good timing between the OPA pump and OPO signal pulses, indicating that the length of the OPA pump path was close to optimal.*

In Figure 3.20, the OPO signal pulse has been scaled up for illustration purposes. The pump pulses and signal pulses were measured with two different detectors that were responsive to 1 μm and 2 μm , respectively. The 2 μm detector turned out to be too slow for the signal pulses. This resulted in a delay of approximately 1.6 ns for the OPO and OPA signal pulses relative to the pump pulses. In Figure 3.20, this has been corrected. To find the exact delay of the signal pulses it was necessary to carry out some additional measurements with the 2 μm detector. These measurements are described in appendix A.

In order to investigate how sensitive the conversion efficiency of the MOPA was to changes in the OPO signal energy, the signal beam was attenuated. The measurements are shown in Figure 3.21.

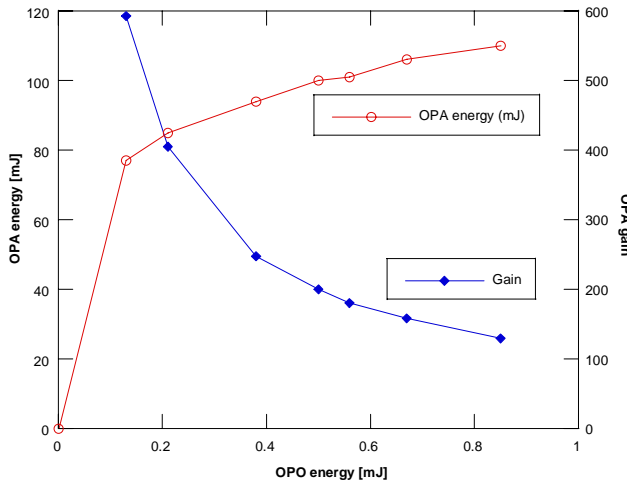


Figure 3.21 *OPA output energy as a function of OPO signal input energy. The OPO produced 1.9 mJ signal energy and the seed energy inside the aperture of the OPA crystals was about 0.9 mJ. The OPA pump energy was 350 mJ ($\sim 2.9 \text{ J/cm}^2$).*

The curves show that the conversion efficiency of the MOPA was relatively unaffected by small changes in the OPO signal energy, e.g. 75 % attenuation of the OPO signal resulted in only 8 % lower MOPA conversion efficiency. As a result, the signal expansion factor was increased. The $f = 150$ mm lens in the signal expansion telescope was replaced with an $f = 200$ mm lens, changing the expansion factor from 6 to 8. Measurements showed that the conversion efficiency of the MOPA configuration was not reduced when the OPO signal beam was expanded by 8, compared to the conversion efficiency with 6 times expansion.

3.2.2 OPA pump energies up to 500 mJ and multiple OPA crystals

As mentioned above, the use of the $f_1 = 750$ mm lens in the relay-imaging telescope gave a beam spot that was too small to utilize maximum pump energy. Due to the limited selection of lenses and the need to control the beam diameter precisely, a lens combination was implemented to obtain an adjustable focal length. The lens combination is shown in Figure 3.22 and consisted of a convex $f = 250$ mm lens and a concave $f = -300$ mm lens separated by a distance of 70 mm. This gave a combination focal length of 625 mm. Photographs of the configuration shown in Figure 3.22 are included in appendix B and lens combination formulas are included in appendix C.

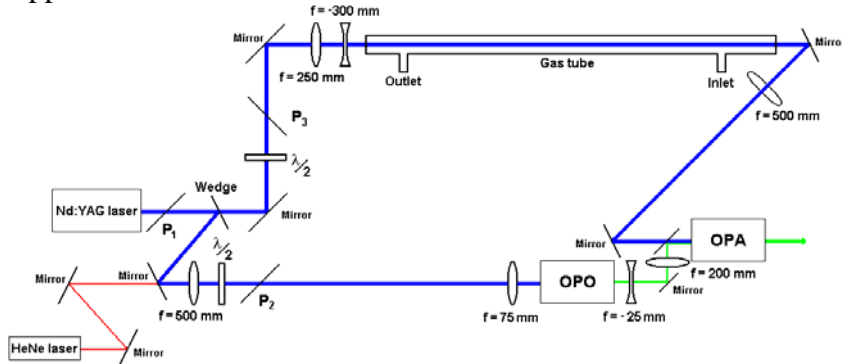


Figure 3.22 The MOPA configuration for OPA pump energies up to 500 mJ. The lens combination $f = 250$ mm and $f = -300$ mm together with the $f = 500$ mm lens of the relay-imaging telescope in the OPA pump path gave a beam diameter of approximately 6.5×5.4 mm² at the OPA crystals.

The last lens in the lens combination was positioned 450 mm before the combination focus and the combination secondary principal plane was 105 mm before the first lens. Also, the object plane of the relay-imaging telescope was now 19 cm behind the laser output aperture. The focal length of the lens combination was 625 mm, giving the relay-imaging telescope a magnification factor of 0.8 and an estimated beam diameter at the OPA crystals of approximately 6.5 mm and 5.4 mm in the horizontal and vertical direction, respectively. The beam almost completely filled the crystal in the horizontal direction.

From measurements of the OPA pump beam with a CCD camera, the peak fluence was estimated to ~ 3 J/cm² at 500 mJ energy. Therefore, the only way to safely exploit the available OPA pump energy of ~ 600 mJ was to use crystals with larger diameters. Since the crystals with 8 mm diameter were the largest ones available in this experiment, the maximum energy the OPA could be pumped with was limited to 500 mJ.

Furthermore, the MOPA was implemented with up to four 15 mm long OPA crystals. The measured and simulated I/O curves for the MOPA with different number of OPA crystals are shown in Figure 3.23.

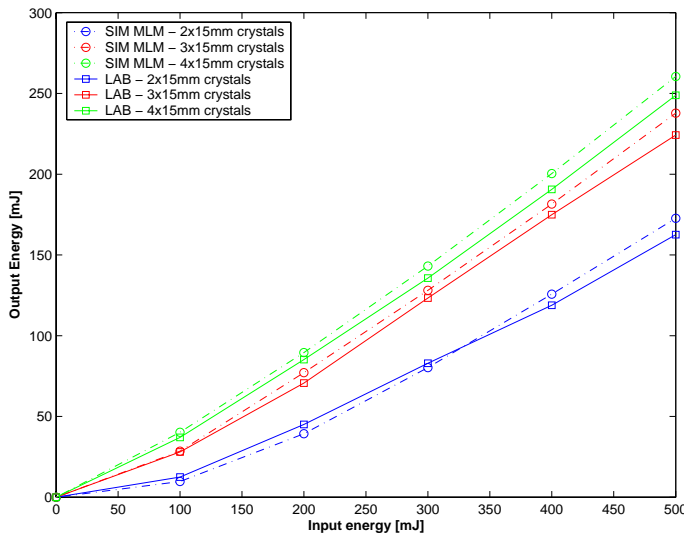


Figure 3.23 The measured and simulated I/O curves for the MOPA configuration with different number of OPA crystals. The pump beam diameter was $6.5 \times 5.4 \text{ mm}^2$ and the signal beam was expanded by a factor 8.

The figure shows good agreement between the implementation in the lab and numerical simulations. The measured conversion efficiencies with 500 mJ input energy were measured to 33 %, 45 % and 52 % (signal and idler) for the MOPA with two, three and four OPA crystals, respectively.

Previous measurements of the output energies, both from the OPO and OPA, had been accomplished with an energy meter that was too slow to register the exact energy in each pulse. In order to estimate statistical fluctuations in the OPA energy output, a pyro-electric energy meter that could measure the energy in each pulse was used and connected to a computer. The computer estimated standard deviation of the MOPA output energy was $\pm 2.56\%$ when operated at 450 mJ and with two OPA crystals. The same method was used to measure the standard deviations of the OPA pump and the OPO signal. The results are shown in Table 3.2 and are all based on an amount of approximately 1000 pulses.

	OPA pump	OPO Signal	OPA signal (2 crystals)
Standard deviation	0.8 %	4.4 %	2.6 %

Table 3.2 Computer estimated standard deviations of OPA pump, OPO signal and OPA signal. The estimations are based on a number of about 1000 pulses.

The energy fluctuation of the OPA signal is less than that of the OPO signal, because the OPA gain saturates at high OPO signal input energy (see Figure 3.21). At lower input energy, there

is larger gain and the energy fluctuation of the OPA signal would be more dependent on the energy fluctuation of the OPO signal.

The fluence distribution of the signal from the MOPA with two, three, and four OPA crystals are shown in Figure 3.24 (a), (b), and (c), respectively.

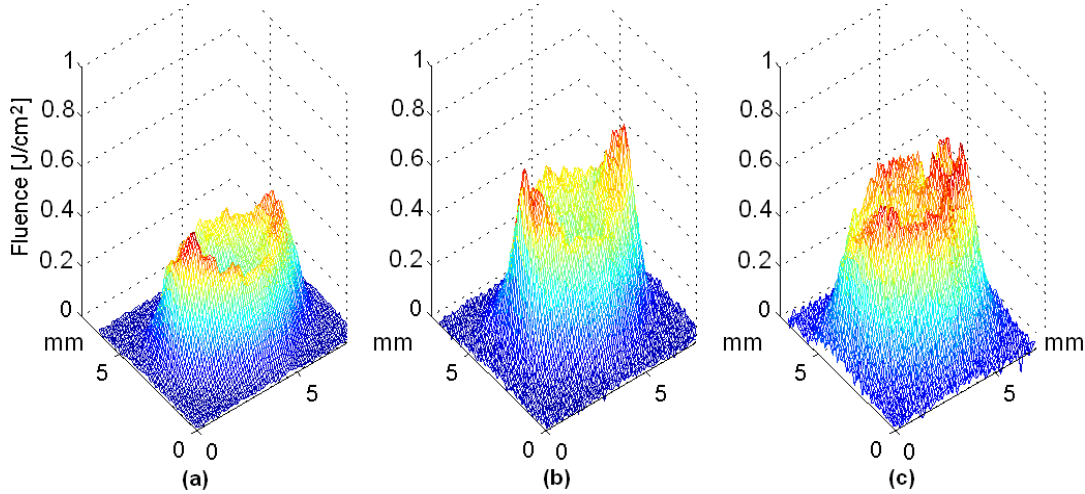


Figure 3.24 The measured fluence distribution of the OPA signal with two (a), three (b), and four (c) 15 mm long OPA crystals. The input energy was 500 mJ and the pictures are taken about 30 cm after the last OPA crystal.

The OPA signal for the MOPA pumped with 500 mJ input energy was characterized by the same method as the beam from the OPO, using an $f = 500$ mm lens to form a waist and an $f = 250$ mm lens to obtain the far field. Table 3.3 summarizes the beam parameters.

MOPA	$d_x \times \theta_x$	$d_y \times \theta_y$	M_x^2	M_y^2	M^2	W_s [mJ]
2 crystals	5.56	7.60	1.9	2.4	2.2	84
3 crystals	12.5	12.0	3.8	3.7	3.8	114
4 crystals	13.7	17.7	4.1	5.2	4.7	133

Table 3.3 Signal beam parameters for various OPA configurations. All the OPAs had 500 mJ of pump energy. The widths d and θ are two times the 16%–84% knife-edge width, and the x and y coordinates correspond to the critical and noncritical directions, respectively. M^2 is an estimate of the overall beam quality, based on the RMS values of the x and y widths. The last column shows the signal energy.

The different transversal parts of the OPA signal obtain different back-conversion and result in the phase front of the beam being distorted. The back-conversion increases as the total crystal length increases and thus correspondingly causes reduced beam quality.

3.3 Summary of experiments

The performances of the linear OPO and the MOPA pumped with three different beam diameters are summed up in Table 3.4.

	Crystal length	Pump energy	Beam diameter	Pump fluence	Efficiency	M^2
OPO	20 mm	8 mJ	$1.2 \times 1.1 \text{ mm}^2$	1.3 J/cm^2	24 % (signal)	2.6
MOPA 1	2x15mm	70 mJ	$2.6 \times 2.5 \text{ mm}^2$	2.2 J/cm^2	37 %	-
MOPA 2	2x15mm	400 mJ	$5.8 \times 4.4 \text{ mm}^2$	3.3 J/cm^2	36 %	-
MOPA 3	2x15mm	500 mJ	$6.5 \times 5.4 \text{ mm}^2$	3.2 J/cm^2	33 %	2.2

Table 3.4 Performances of the linear OPO and the MOPA pumped with different beam diameters. The beam diameters were estimated on basis of 90 % encircled energy.

The conversion efficiencies of the three MOPAs pumped with different beam diameters are shown in Figure 3.25.

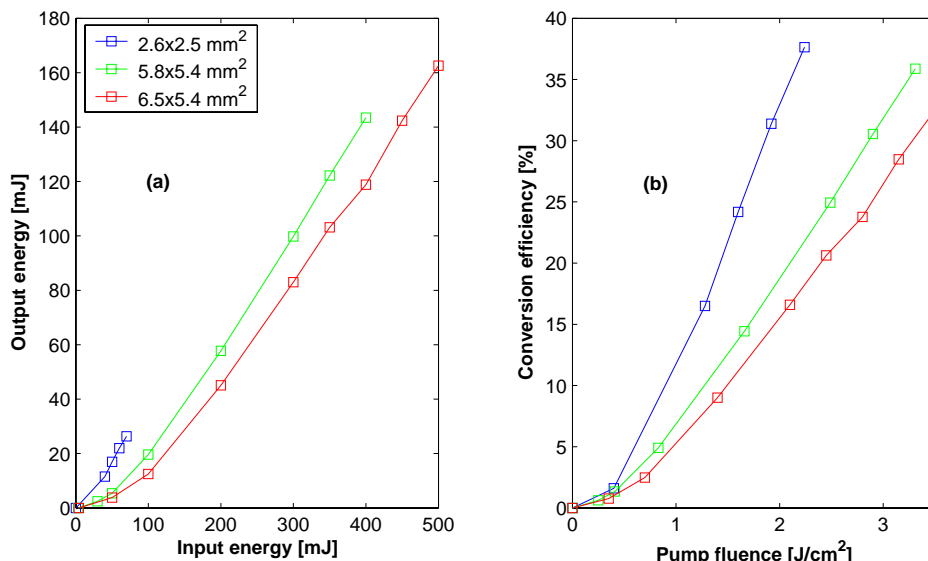


Figure 3.25 I/O curves (a) and conversion efficiencies as a function of pump fluence (b) for the MOPA pumped with different beam diameters. The conversion efficiency was better for small OPA pump beam diameters.

The MOPA efficiency seems to decrease with increasing beam diameters. The reasons for this are not fully understood. One reason may be that less OPO signal energy enters the OPA stage as the expansion of the OPO signal is increased.

Table 3.5 summarizes the performance of the MOPA with different number of OPA crystals.

Crystal length	Efficiency	M^2
2x15 mm	33 %	2.2
3x15 mm	45 %	3.8
4x15 mm	52 %	4.7

Table 3.5 Performance of the MOPA with different number of OPA crystals. The pump energy was 500 mJ and the pump beam diameter was $6.5 \times 5.4 \text{ mm}^2$.

3.4 Instrumentation

Lasers:

- Quantel Brilliant B, Q-switched Nd:YAG-laser, 10 Hz pulse rate, $\lambda = 1064 \text{ nm}$, $E_{\max} = 900 \text{ mJ}$, 5 ns pulse duration.
- Melles Griot, 0,5 mW HeNe-laser, vertically polarized, Model number 05-SRP-812-230.

Polarizers:

- P1: Thin Film Polarizer at 1064 nm/57°, 27 × 50 × 1.5 mm.
- P2: CVI Polarizer, 1064 nm/57°.
- P3: Layertec Polarizer, 1064 nm/45°.

Wave retarders:

- CVI laser corporation, $\lambda/2@1064\text{nm}$.
- Altechna, $\lambda/2@1064\text{nm}$.

Folding mirrors:

- New Focus 5104, HR@1064 nm
- Layertech, 100717, HR(45°, 1030-1064 nm) > 99.9 %, AR@1064nm.
- Laseroptik, HT 1064 nm and 2168 nm/45°P, HR 2090 nm/45° S-pol, Ø 25 x 6.35 mm.

OPO mirrors:

- Laseroptik, notch filter, HT 1064 nm and 2170-2260 nm/0°, HR 2010-2090 nm/0°, AR@1064 nm/0°.
- Laseroptik, HT 2170-2260 nm/0°, HR 1064 nm + R = 80 % 2010-2090 nm/0°, AR@2010 - 2260nm/0°.

Lenses:

- ThorLabs, 1" diameter BK7 lens kit, AR-coated at 600-1050 nm.
- Casix, 1" diameter CaF₂ lens kit, AR@2000 nm.

Crystals:

- OPO: Cristal Laser S.A, KTP 4×4×20 mm, $\theta = 50.5^\circ$, $\phi = 0^\circ$.
- OPA: Cristal Laser S.A, KTP 8×8×15 mm, $\theta = 50.5^\circ$, $\phi = 0^\circ$.

Cameras:

- Spiricon Inc, Silicon CCD-camera, Model No: TC-1152.
- Spiricon Inc, Pyro-electrical camera, Model No: PY-128x128B.

Measuring equipment:

- Energy meter
- Spectrometer
- Oscilloscope
- Diode-detectors

4 SIMULATIONS

The design of the MOPA system was based on single-longitudinal mode simulations performed in the project assignment. Still, as the system was being implemented in the lab, changes had to be made because the mirrors of the ring OPO turned out to have too low damage threshold. For this reason, the linear OPO was built, using mirrors with higher damage threshold. However, the poor performance of the linear OPO in the lab resulted in the implementation of the relay-imaging telescope in the OPO pump path, in order to improve the transversal distribution of the pump beam. Obviously, these changes to the system required additional simulations to be carried out. Also, multi-longitudinal mode pump had to be used for more realistic simulation of the configuration.

4.1 The simulation model

The simulation model Sisyfos (Simulation system for OPO science) has been developed at FFI. It is an object-oriented program running under MatLab. There are objects corresponding to the optical components (such as mirrors, nonlinear crystals, and air gaps) as well as objects for beam sources and storage of simulation results. The user can simulate an optical device, e.g. a laser or an OPO, by creating a list of objects corresponding to the components of the device and then run the main simulation program on that list.

The optical beams are represented by 3D arrays that represent the complex amplitude as a function of transverse coordinates and time. The optical carrier wave is factored out, so the arrays represent the amplitudes of the envelope functions. An amplitude array represents the beam at a specific longitudinal position. The objects that represent optical components have associated functions that transform a beam array in a way that corresponds to propagation through the component. Calling such functions in sequence simulates beam propagation through the whole device.

The central part of the model is the object representing the nonlinear crystal. This can handle the second-order nonlinear interaction between two or three beams as well as absorption and thermal effects. All the relevant physical effects, such as diffraction, dispersion, birefringent walk-off and pump depletion are taken into account.

4.2 Previous simulations

The most important simulations performed in the project assignment are summarized in the following [13]. Figure 4.1 shows the efficiencies (signal) and beam qualities of a ring OPO pumped with 2, 4, 6, and 8 mm beam diameters. In each case, the maximum pump energy is chosen so that the total fluence in the OPO is approximately 3 J/cm^2 . The OPO mirrors were assumed to be ideal (i.e. totally transmitting or reflecting) in these simulations, i.e. the OPO was singly resonant. The signal output coupling was 50 %.

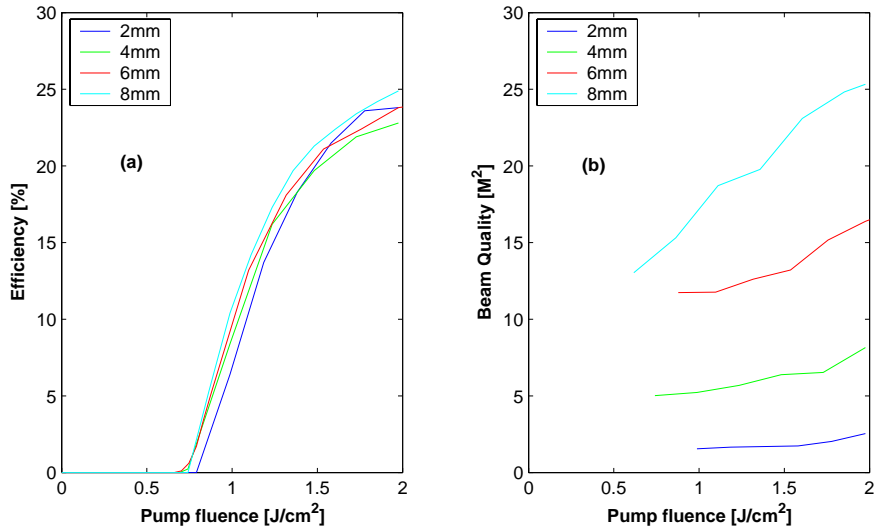


Figure 4.1 Simulated signal conversion efficiencies (a) and beam qualities (b) for a ring OPO pumped with different beam diameters, but with the same pump fluence. The signal output coupling was 50 % and two crystals with length 20 mm were used. The beam qualities shown were the second moment M^2 in the non-critical direction. The beam qualities in the critical direction were considerably better.

The graphs show that the conversion efficiency is nearly independent of the beam diameter, whereas the beam quality dramatically worsens as the beam diameter increases. To conclude, traditional flat mirror OPOs are not suited for conversion of high-energy pulses when high beam quality is required.

The simulations parameters and simulated performance of the MOPA system designed in the project assignment are repeated in Table 4.1. All simulations were carried out with a pump that had an asymmetric Gaussian pulse shape with 2 ns rise time and 3 ns fall time and single-longitudinal mode.

	Crystal length	Pump energy	Beam diameter	Fluence	Efficiency	M^2
OPO	20 mm	11 mJ	1 mm	2.9 J/cm^2	16 % (signal)	1,4
OPA	2x15 mm	600 mJ	6 mm	2.7 J/cm^2	48 %	1,6

Table 4.1 Simulation parameters and performance of the MOPA system designed in the project assignment. Single-longitudinal mode pump was used in the simulations. The beam quality is based on the second moment M^2 .

The ring OPO was pumped with a far field fluence distribution of the laser beam (Figure 3.2), whereas the OPA was pumped with a scaled version of the near-field fluence distribution of the laser beam. The optimal time delay of the OPA pump pulse was 2.6 ns and the OPO signal beam was expanded by a factor 8 before entering the OPA stage.

A single-longitudinal mode pump was used in the project assignment simulations, mainly to reduce the time consumption of each simulation. During the implementation of the MOPA, it was discovered that this simplification lead to substantial deviation from the experimental results with real, multi-longitudinal mode pump beam (the pump laser has a bandwidth). For example, single-longitudinal mode simulations showed that the optimal total OPA crystal length for maximum conversion efficiency was about 35 mm (at longer crystal lengths, back-conversion limited the conversion efficiency). The available crystals in the lab were all 15 mm long, so the MOPA was implemented with two crystals in the preliminary experiments. However, this turned out not to be the optimal OPA crystal length with a multi-longitudinal mode pump. For this reason, the simulations were repeated with a multi-longitudinal mode pump.

4.3 New simulations

All the new simulations used a multi-longitudinal mode pump. The pump pulse was created from a Gaussian envelope multiplied by a modulation pattern corresponding to multiple modes with random complex amplitudes and a spectrum with 20 GHz FWHM.

4.3.1 Linear OPO

The linear OPO was implemented in the lab because of the poor performance of the ring OPO. In order to make the simulations of the linear OPO as realistic as possible the real frequency dependence of the mirrors was taken into account. Table 4.2 shows the reflectance coefficients of the mirrors used in the simulations of the linear OPO.

	Idler	Signal	Pump
Mirror 1	0.1	0.995	0.002
Mirror 2	0.06	0.74	0.998

Table 4.2 Reflectance coefficients of the mirrors used in the simulations of the linear OPO.

The values are collected from the measured frequency response of the mirrors. Those are included in appendix D and show that the pump was not completely transmitted at mirror 1. To prevent multiple reflections of the pump inside the simulated linear resonator, which makes the simulations unnecessarily complicated, the pump reflectance in mirror 1 was set to 0 (full transmittance). To compensate for this approximation, the amount of input energy was reduced by 5 %.

First, the linear OPO was pumped with the same far field fluence distribution that was used to pump the ring OPO. As mentioned in Chapter 3, lab measurements showed poor performance of the linear OPO pumped with this far field fluence distribution. This resulted in the implementation of the linear OPO pumped with a relay-imaged fluence distribution. Table 4.3 shows the simulation parameters of the linear OPO pumped with the two different fluence distributions. The total fluence in the resonator was around 2 J/cm^2 (restricted by the damage threshold of the OPO mirrors).

Fluence distribution	Pump energy	Beam diameter	Fluence	Efficiency (signal)	M_x^2	M_y^2
Far field	8 mJ	1 mm	2.0 J/cm^2	27 %	1.6	1.3
Relay-image	8 mJ	1.2 mm	1.9 J/cm^2	26 %	1.5	1.3

Table 4.3 Simulation parameters and performances of the linear OPO pumped with two different fluence distributions and with multi-longitudinal mode pump. One KTP crystal of length 20 mm was used in both cases.

The table shows that the simulated conversion efficiency and beam quality were nearly the same for the linear OPO pumped with far field and relay-imaged fluence distributions. As it was shown in Figure 3.16, the measured performance of the two linear OPOs differed significantly in the lab.

Figure 4.2 shows the simulated I/O curves for the linear OPO pumped with the two different fluence distributions for both single- and multi-longitudinal mode pump.

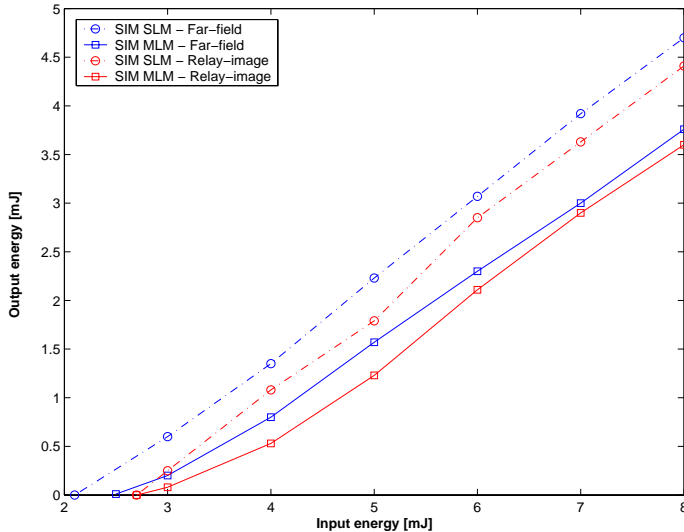


Figure 4.2 Simulated I/O curve for the linear OPO pumped with different fluence distributions. Both simulations with single- (SLM) and multi-longitudinal mode (MLM) pump are shown. The total output energy (idler + signal) is plotted and the idler energy was about ¾ of the signal energy.

The multi-longitudinal mode simulations gave lower conversion efficiencies than those with single-longitudinal mode, because the pulse modulation leads to strong back-conversion during high peaks and also to longer build-up time.

4.3.2 The MOPA configuration

The MOPA configuration was optimized through simulations with a multi-longitudinal mode pump. Figure 4.3 shows the simulated conversion efficiency of the MOPA as function of time delay of the OPA pump, both for single- and multi-longitudinal mode simulations.

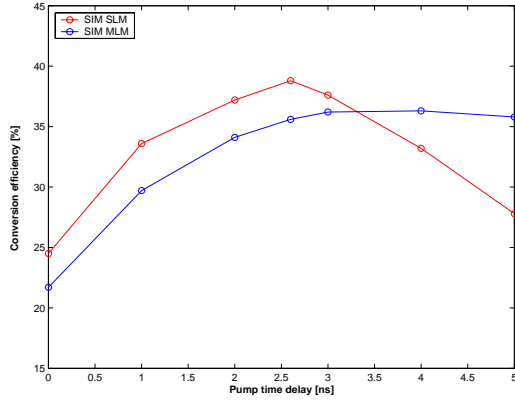


Figure 4.3 Simulated conversion efficiency of the MOPA as function of the pump time delay for both single- (SLM) and multi-longitudinal mode (MLM) pump. Two 15 mm long KTP crystals were used in the OPA and the input pump energy was 500 mJ in all the simulations. The OPO signal was expanded by a factor 8 before passed on to the OPA crystals.

The single-longitudinal mode simulations clearly show an optimal OPA pump time delay of about 2.6 ns. The optimal point is less distinguishable for the multi-longitudinal mode curve and a time delay between 2.5 and 5 ns seems to have little effect on the conversion efficiency.

The conversion efficiency of the MOPA as function of total OPA crystal length is shown in Figure 4.4.

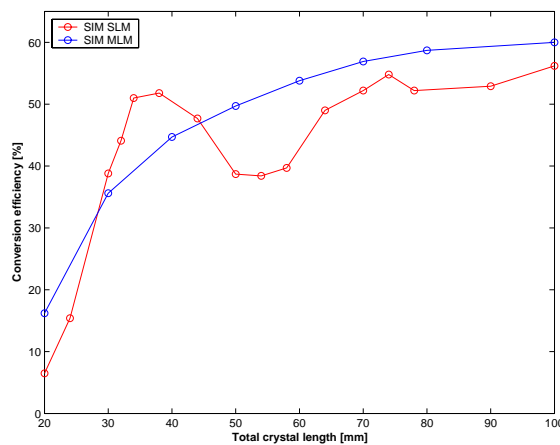


Figure 4.4 Simulated conversion efficiency of the MOPA as function of total OPA crystal length for both single- (SLM) and multi-longitudinal mode (MLM) pump. The OPA pump time delay was 2.6 ns and the OPA pump energy was 500 mJ in all the simulations.

The multi-longitudinal mode curve shows that back-conversion gradually increases and that the conversion efficiency seems to approach a limit of about 60 %. The single-longitudinal mode simulations on the other hand indicate strong back- and forward-conversion where the conversion efficiency starts to oscillate for total crystal lengths above \sim 35 mm. This can also

be seen from the shape of the MOPA pulses when the total OPA crystal lengths are 30 mm and 50 mm, shown in Figure 4.5 (a) and (b), respectively.

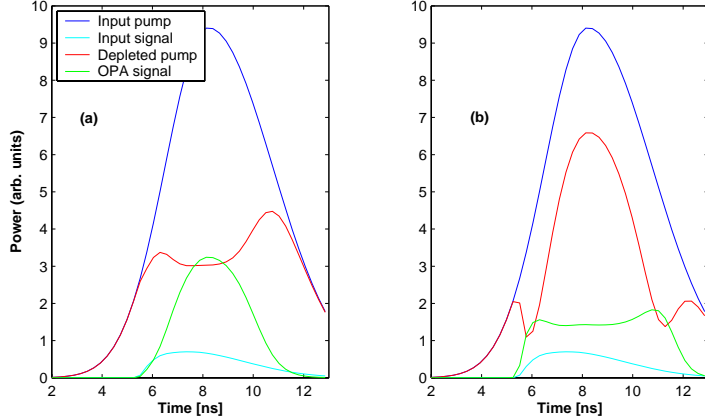


Figure 4.5 Simulated time evolution of the pulses in the MOPA with a single-longitudinal mode OPA pump and OPO signal. With two 15 mm long OPA crystals (a) there was no back-conversion of the OPA signal, whereas with two 25 mm crystals (b) there was strong back-conversion.

The I/O curve for the MOPA with two, three, and four 15 mm long OPA crystals are shown in Figure 4.6 for simulations with both single- and multi-longitudinal mode pump.

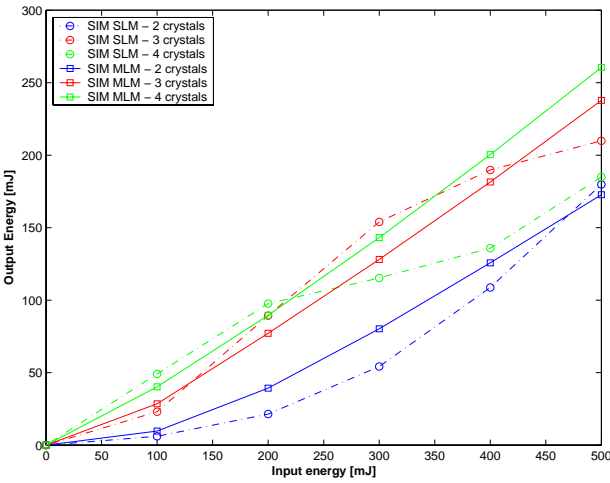


Figure 4.6 Simulated I/O curves for the MOPA with different number of OPA crystals for both single- (SLM) and multi-longitudinal mode (MLM) pump. For the SLM pump, there was strong back-conversion in the cases when three and four crystals were used.

There are striking differences between the curves for the single-longitudinal mode and multi-longitudinal mode pumps. Because the gain in the nonlinear crystal is proportional to $\exp(I)$, where I is the intensity of the pump, the curve has an exponential form at low conversion. This can be observed in Figure 4.6 in the curve for the single-longitudinal mode pump and two OPA crystals. At higher energies, saturation will stop the exponential growth. Too high energies will result in reduced conversion efficiency, due to back-conversion. This can be seen for three and four crystals at pump energies of 300 mJ and 200 mJ, respectively.

The curves for the multi-longitudinal mode pump shown in Figure 4.6 are more complicated to describe. Some spikes may have saturation or back-conversion, whereas other parts of the pulse have low conversion. The total conversion efficiency is averaged over a wide range of intensities occurring in the pulse. The result is that the curves for the multi-longitudinal mode pump are approximately linear within the interval shown in Figure 4.6. From the figure it is obvious that in simulations of the OPA, the multi-longitudinal mode nature of the pump is of great importance.

The simulated OPA signal fluence distributions for two, three, and four OPA crystals and with are shown in Figure 4.7 (a), (b), and (c), respectively. The normalized fluence distribution of the OPA signal did not change much when the number of OPA crystals was increased.

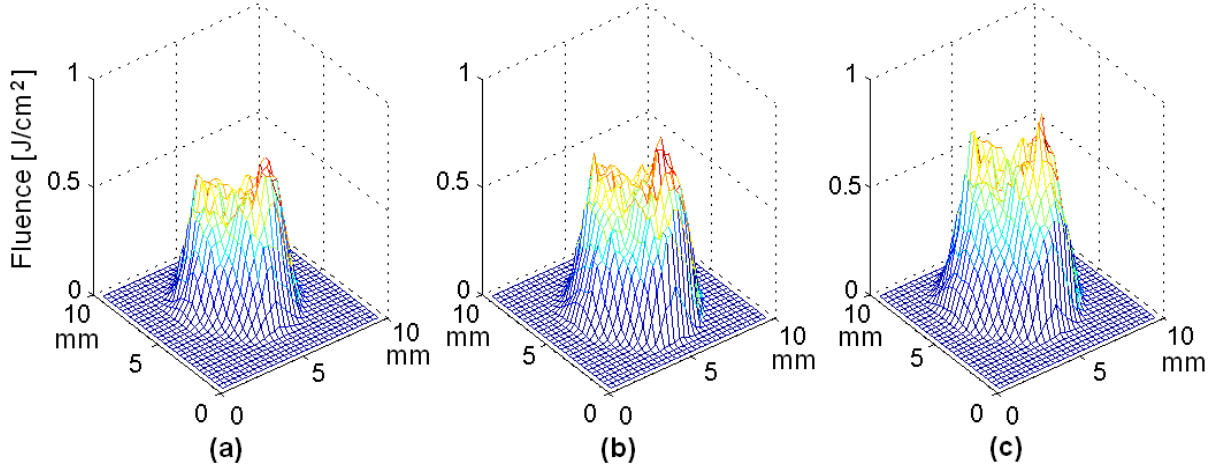


Figure 4.7 Simulated fluence distribution of the OPA signal at 500 mJ pump energy with two 15 mm OPA crystals (a), three 15 mm OPA crystals (b), and four 15 mm OPA crystals (c). Multi-longitudinal mode pump was used.

The beam quality of the simulated OPA signal was estimated using the same method as used in the lab. The results are shown in Table 4.4.

MOPA	$d_x \times \theta_x$	$d_y \times \theta_y$	M_x^2	M_y^2	M^2	$W_s [\text{mJ}]$
2 crystals	4.96	4.80	1.7	1.6	1.7	88.2
3 crystals	6.28	6.28	2.1	2.1	2.1	121.4
4 crystals	10.08	9.2	3.1	2.9	3.0	132.8

Table 4.4 Signal beam parameters for various OPA configurations. All the OPAs had 500 mJ of pump energy. The widths d and θ are two times the 16%–84% knife-edge width, and the x and y coordinates correspond to the critical and noncritical directions, respectively. M^2 is an estimate of the overall beam quality, based on the RMS values of the x and y widths. The last column shows the signal energy.

The simulated performances of the MOPA configuration with two, three, and four 15 mm long OPA crystals are summarized in Table 4.5.

MOPA	Crystal length	Pump energy	Beam diameter	Fluence	Efficiency	M^2
Simulations	2x15 mm	500 mJ	6.5x5.4 mm ²	2.9 J/cm ²	36.0 %	1.7
Simulations	3x15 mm	500 mJ	6.5x5.4 mm ²	2.9 J/cm ²	47.6 %	2.1
Simulations	4x15 mm	500 mJ	6.5x5.4 mm ²	2.9 J/cm ²	52.1 %	3.0

Table 4.5 Simulations parameters and simulated performance of the MOPA with multi-longitudinal mode pump and different number of OPA crystals.

The table shows that the simulated conversion efficiency of the MOPA increased and the beam quality of the OPA signal deteriorated as the total OPA crystal length was increased.

5 DISCUSSION

Both simulations and experiments have shown that there is a trade-off between the conversion efficiency and the beam quality of the MOPA. This is illustrated in Figure 5.1.

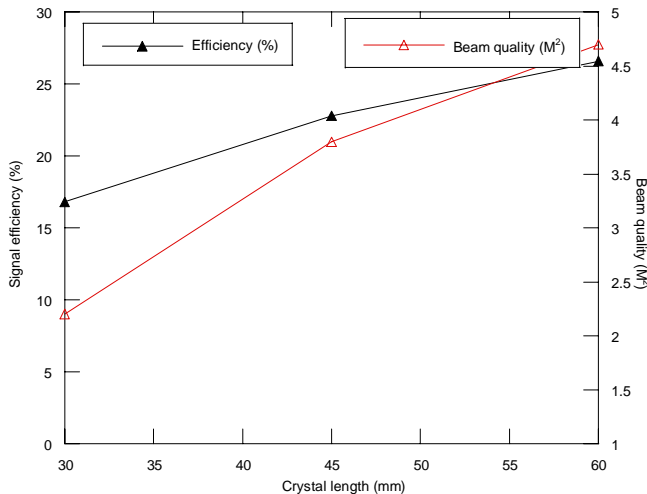


Figure 5.1 The measured signal conversion efficiency and signal beam quality of the MOPA as a function of total OPA crystal length. 15 mm long crystals were used in the experiment and the measurements were made when two, three, and four OPA crystals were used in the MOPA.

As the total crystal length of the OPA increases, the conversion efficiency improves, whereas the beam quality worsens.

5.1 Optimization of the conversion efficiency

The measured conversion efficiency of the MOPA complied well with the simulated conversion efficiency. However, there are some parameters that may not be optimal in the MOPA configuration, thus reducing the overall conversion efficiency.

The dependence of the conversion efficiency of the MOPA on the time delay of the OPA pump has not been inspected in the implementation, but the measured time delay (see Figure

3.20 on page 36) indicate relatively good timing of the OPA pump. Also, Figure 4.3 showed that the pump time delay of the simulated MOPA had a relatively wide interval in which the conversion efficiency varied slowly. Thus, it is reasonable to believe that the present length of the OPA pump path is nearly optimal.

The transversal distribution of the OPA pump beam was slightly asymmetric. This asymmetry could arise from the laser itself or from the Brewster windows of the vacuum tube. With this asymmetric OPA pump beam, it is not possible to fill the OPA crystals in both transversal directions.

Measurements made in the lab showed that the total conversion efficiency of the MOPA with two OPA crystals was lowered from 32 % to 31 % when the OPO signal energy was decreased by 10 %. As the total OPA crystal length increases, the back-conversion becomes stronger. Thus, increasing the OPO signal energy will not result in improved conversion efficiency of the MOPA with long OPA crystal length.

There is a possibility of inserting mirrors that couple the idler out between the OPA crystals. Simulations predicted that for the MOPA with four crystals, the OPA signal energy was increased by 30 % when the idler was coupled out between the third and fourth OPA crystal. The reason for the improvement is that the back-conversion of the OPA signal is reduced when some of the idler energy is removed. However, outcoupling of the idler between the third and fourth OPA crystal in the lab gave only about 8 % more OPA signal output energy.

5.2 Optimization of the beam quality

There are also several ways to improve the beam quality of the OPA signal. However, there is a trade off between the conversion efficiency and the beam quality of the OPO, as it is for the MOPA system.

Simulations indicated that output coupling of the idler between the OPA crystals will, in addition to increase the OPA signal energy improve the beam quality of the OPA signal. The measured results in the lab are summarized in Table 5.1 and indicate that output coupling of the idler between the third and fourth OPA crystal could be favorable in applications where the idler is not exploited.

Number of OPA crystals	Idler output coupling	Signal energy [mJ]	M^2
3	None	114	3.8
3	After 2 nd crystal	121	2.3
4	None	133	4.7
4	After 3 rd crystal	143	4.5
4	After 2 nd & 3 rd crystal	138	2.3

Table 5.1: Measured performance of the MOPA when the idler is coupled out at different locations in the OPA. The pump energy was 500 mJ and the OPA crystals were 15 mm long.

As mentioned in section 2.3.3, the most divergent components of the OPO signal are not passed on to the OPA. However, the beam quality of the OPO signal was not very good ($M^2 \approx 2.6$) and may have contributed to reduce the beam quality of the OPA signal. Since the conversion efficiency of the OPO is of minor importance in the MOPA configuration with long OPA crystal length, it is possible to make adjustments to the OPO that improve the beam quality of the OPO signal at the expense of some lower conversion efficiency. The beam quality of the OPO signal can be improved by several methods. The easiest way is probably to decrease the diameter of the OPO pump beam. A narrow pump beam produces a narrow gain region that acts as an aperture. Thus, the signal beam components with large angles obtain limited amplification, resulting in a narrow signal beam with low divergence, as explained in section 2.3.1. Another way to increase the beam quality of the signal is to increase the distance between the OPO mirrors, which is illustrated in Figure 5.2.

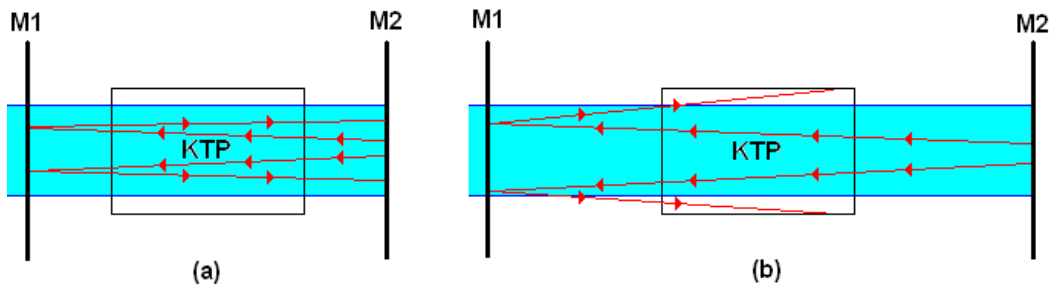


Figure 5.2 The linear OPO with small airgaps (a) and with relatively long airgaps (b). Longer airgaps prevent the most divergent angle components of the signal from oscillating.

When the spacing between the mirrors is increased, the most divergent angle components of the signal fail to oscillate and will not contribute to the output signal. Thus, the OPO signal becomes less divergent and the beam quality is improved, whereas the conversion efficiency of the OPO decreases as the build-up time is increased.

5.3 General comments on the MOPA system

One of the greatest advantages of the MOPA system is that the OPA is easily scaleable. The limiting factors in this work have been the energy of the pump laser and the transversal area of the OPA crystals. The performance of the MOPA pumped with different pump beam diameters has indicated that the conversion efficiency is reduced as the beam diameter increases. There is no fundamental reason that this should happen. It is probably caused by reduced seed intensity (less OPO signal energy) and changes in the pump beam profile.

The MOPA configuration is also well suited for efficient conversion of short pulses (~6 ns). Generally, short pulses have fewer roundtrips in the OPO resonator and this leads to poor beam quality of the OPO signal. In the MOPA configuration, the beam quality of the MOPA signal is not that dependent on the beam quality of the OPO signal, because the most divergent parts of the OPO signal beam never enter the OPA stage. This makes it possible to obtain both high conversion efficiency and high beam quality for short pulses.

5.4 Deviations between lab measurements and simulations

The deviations between performance of the implemented and simulated configuration can probably be ascribed to approximations and assumptions made in the simulation parameters. The lenses and crystals in the implemented configuration may exhibit imperfections in the AR-coatings. Measurements of the nonlinear susceptibility of the crystals often differ by 10 % or more and constitute a major uncertainty. The crystals in the lab may also have inhomogeneities that cannot be represented accurately in the simulation model.

The Nd:YAG laser source is in the simulations assumed to be separable in time and in transversal spatial distribution. This is a considerable approximation for this type of laser [15]. Also, the direction and the fluence distribution of the pump in the lab fluctuate from pulse to pulse. It is possible to include these fluctuations in the simulations, but it requires much effort.

The pulse shape and pulse energy from the Nd:YAG laser fluctuate, whereas each simulation is performed with an identical representation of the pulse. The simulated pulse shape is Gaussian distributed and deviates from the pulse shape measured in the lab, both shown in Figure 5.3.

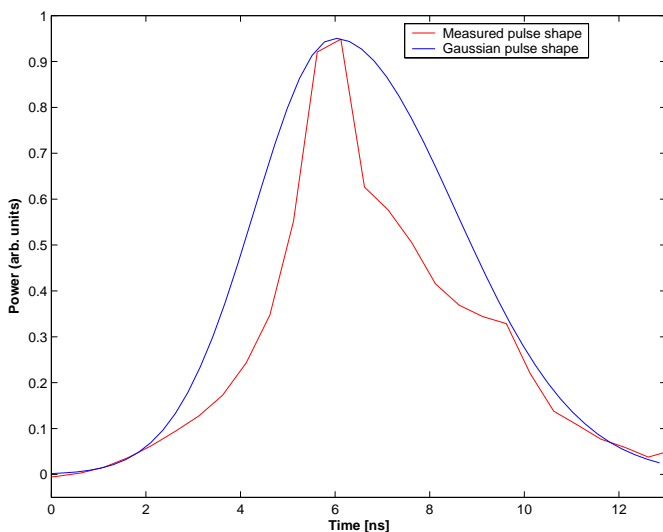


Figure 5.3 The measured pulse shape and the Gaussian distributed pulse used to represent the pulse shape in the simulations.

Simulations with the measured pulse shape were performed at a late stage and showed no substantial reduction of the MOPA performance.

5.5 Plans ahead

As explained in the introduction, the purpose of the 2 μm MOPA system is to reach the 3-5 μm or 8-12 μm wavelength ranges. This can be achieved by implementing a system, where both the 2080 nm signal and 2173 nm idler from the MOPA in this work are utilized, shown in Figure 5.4.

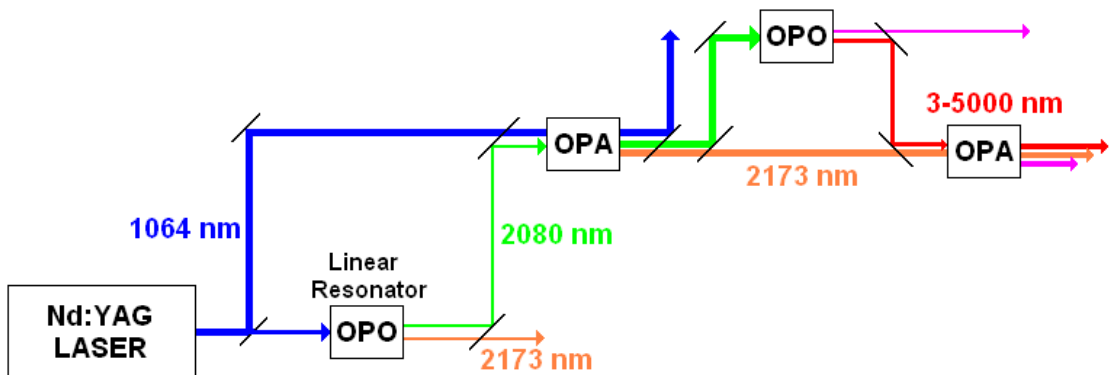


Figure 5.4 System architecture for conversion from 1 μm to the 3-5 or 8-12 μm wavelength ranges.

An OPO converts the signal of the first MOPA to a longer wavelength. The OPO signal is then amplified in an OPA pumped with the idler of the first MOPA.

6 CONCLUSION

Conversion of high-energy pulses from 1 μm to 2 μm has been demonstrated in a master oscillator/power amplifier (MOPA) architecture. The system was characterized experimentally and a conversion efficiency of 52 % (signal and idler) and a beam quality of $M^2 \approx 2.3$ were obtained when pumped with 500 mJ. The experimental results complied well with numerical simulations of the configuration.

One of the challenges of constructing the configuration was to obtain a good transversal distribution of the pump. For this purpose, relay-imaging telescopes were used in the pump paths to transfer the nearly flat-topped transversal distribution inside the pump laser to the nonlinear crystals in both the OPO and the OPA.

The OPA was implemented with two, three, and four 15 mm long KTP crystals. The conversion efficiency improved and the beam quality worsened, as the total crystal length of the OPA was increased. Simulations predicted that the conversion efficiency and beam quality of the OPA signal should improve when the idler was filtered out between the OPA crystals, and these improvements were also seen in the experiments.

The results demonstrate that the MOPA system can combine high efficiency and acceptable beam quality even for pulses of only a few nano-seconds. Furthermore, the MOPA system is more suitable for scaling than an OPO.

APPENDICES

A DETERMINATION OF TIME DELAY IN THE 2 μm DETECTOR

Additional experiments were performed in the laboratory to investigate the delay of the 2 μm detector used to measure the signal pulse shapes in Figure 3.20. One way to make an exact measurement of the delay was to insert a KTP crystal after the OPA in the experimental setup shown in Figure A.1.

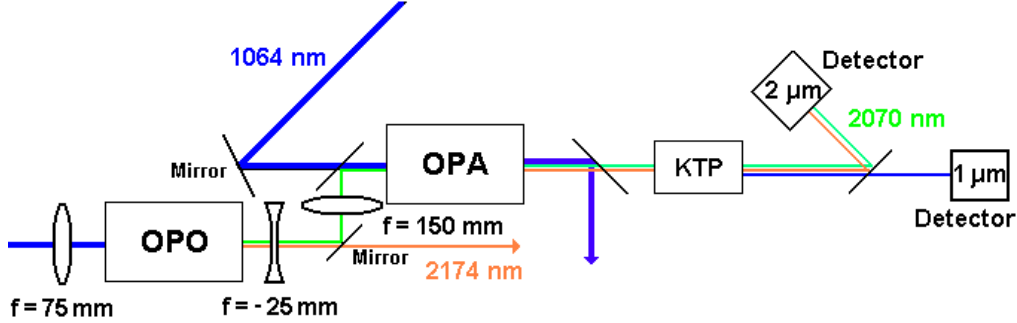


Figure A.1 Experimental setup for investigation of the 2 μm detector delay. The beam propagation distances from the KTP crystal to the two detectors were equal.

The nonlinear interaction process between the signal and idler in the KTP gave rise to sum-frequency generation, where a third wave was generated having a frequency equal to the original Nd:YAG laser (1.064 μm). The three pulses then left the KTP crystal at the exact same time, making it possible to measure the time delay of the 2 μm detector relative to the 1 μm detector with high certainty. In addition, the lengths of the coax cables from the two detectors to the oscilloscope were equal. The measured pulses are shown in Figure A.2.

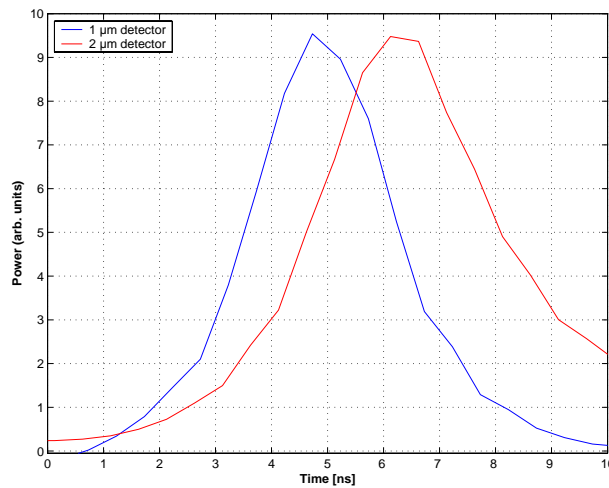


Figure A.2 Measured pulses to determinate the delay of the 2 μm detector relative to the 1 μm detector.

The figure shows that the delay of the 2 μm detector relative to the 1 μm detector was approximately 1.5 ns. Compared to the Nd:YAG pulse duration of 5 ns, this time delay was quite influential on the pulse measurements shown in Figure 3.20.

B PHOTOGRAPHS OF THE IMPLEMENTATION IN THE LAB

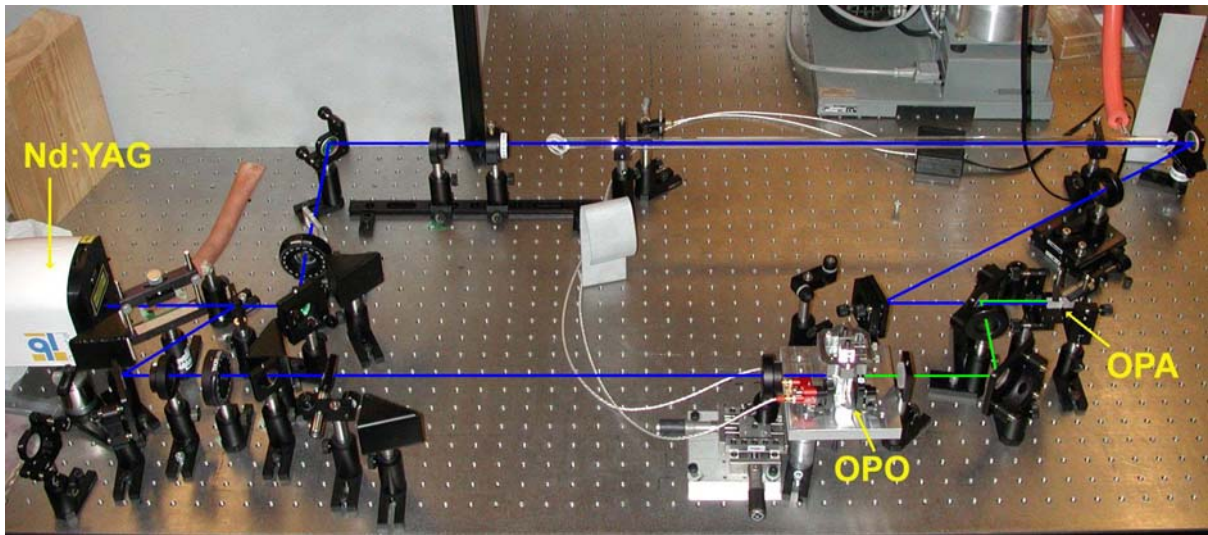


Figure B.1 The MOPA configuration (also shown in Figure 3.22).

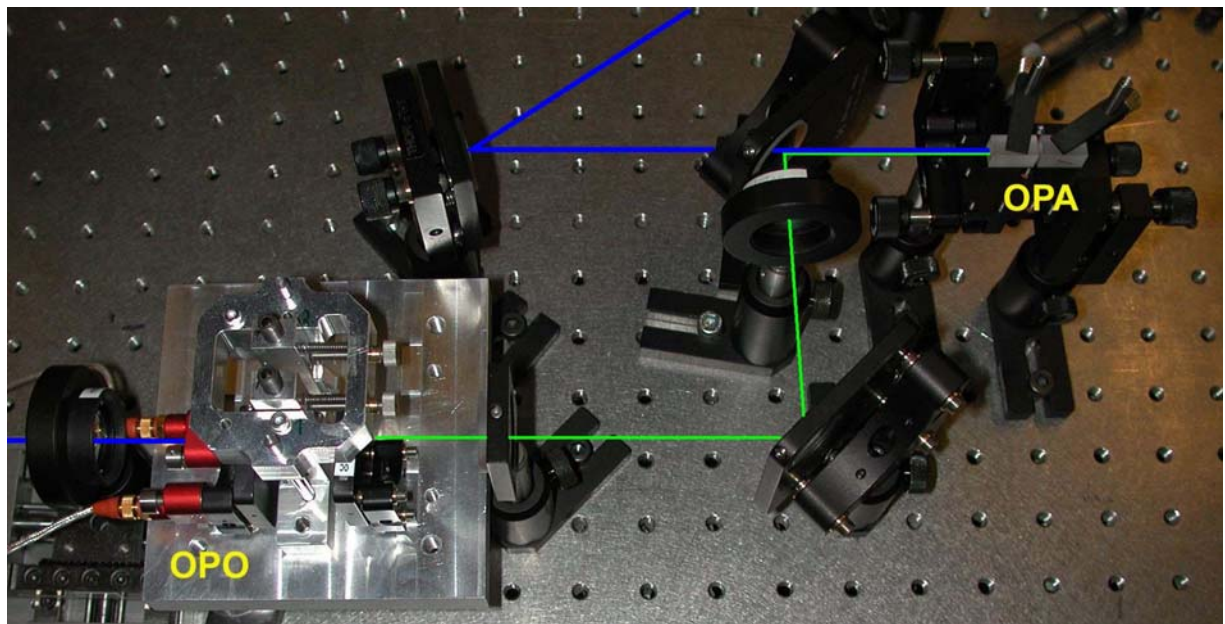


Figure B.2 Zoom in of the linear OPO and the OPA with two 15 mm long KTP crystals.

C LENS COMBINATION FORMULAS

In optical systems, it is often necessary to combine lenses in order to obtain focal lengths that are not available from conventional production line lenses. The combination focal length of a two-element lens combination is given by

$$f = \frac{f_1 f_2}{f_1 + f_2 - d}, \quad (\text{C.5})$$

where f_1 is the focal length of the first element, f_2 is the focal length of the second element and d is the distance from the secondary principal point of the first element to the primary principal point of the second element.

The position of the combination focal point relative to the secondary principal point of the secondary element is

$$f' = \frac{f_2(f_1 - d)}{f_1 + f_2 - d}, \quad (\text{C.6})$$

and the distance the secondary principal point of the secondary element is moved by being part of the combination is given by

$$z = f - f'. \quad (\text{C.7})$$

Figure C.1 shows the above-mentioned variables for a telephoto combination having a convex and a concave lens as first and secondary element, respectively.

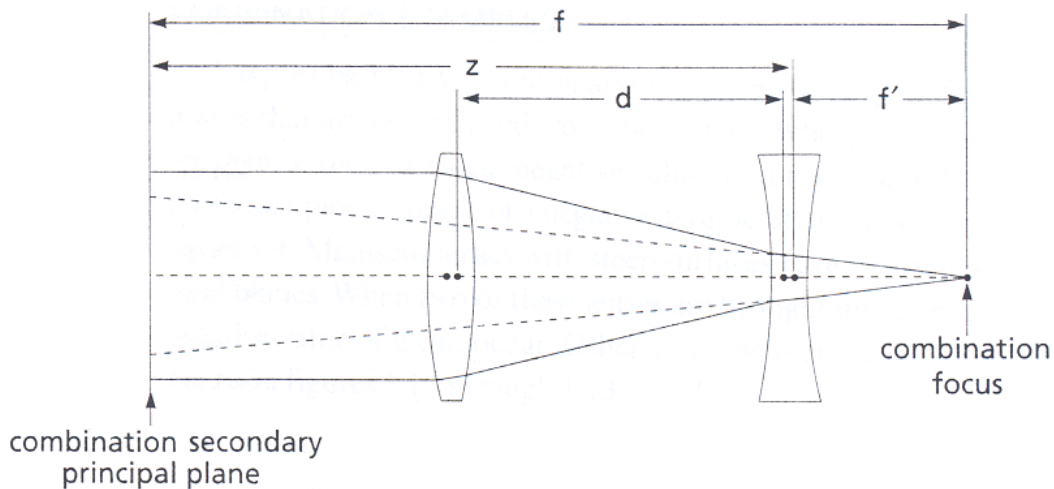


Figure C.1 A two-element lens combination consisting of a convex and a concave lens, also known as a telephoto combination. Increasing or decreasing the distance between the lenses adjusts the combination focus.

D TRANSMISSION CHARACTERISTICS OF THE OPO MIRRORS

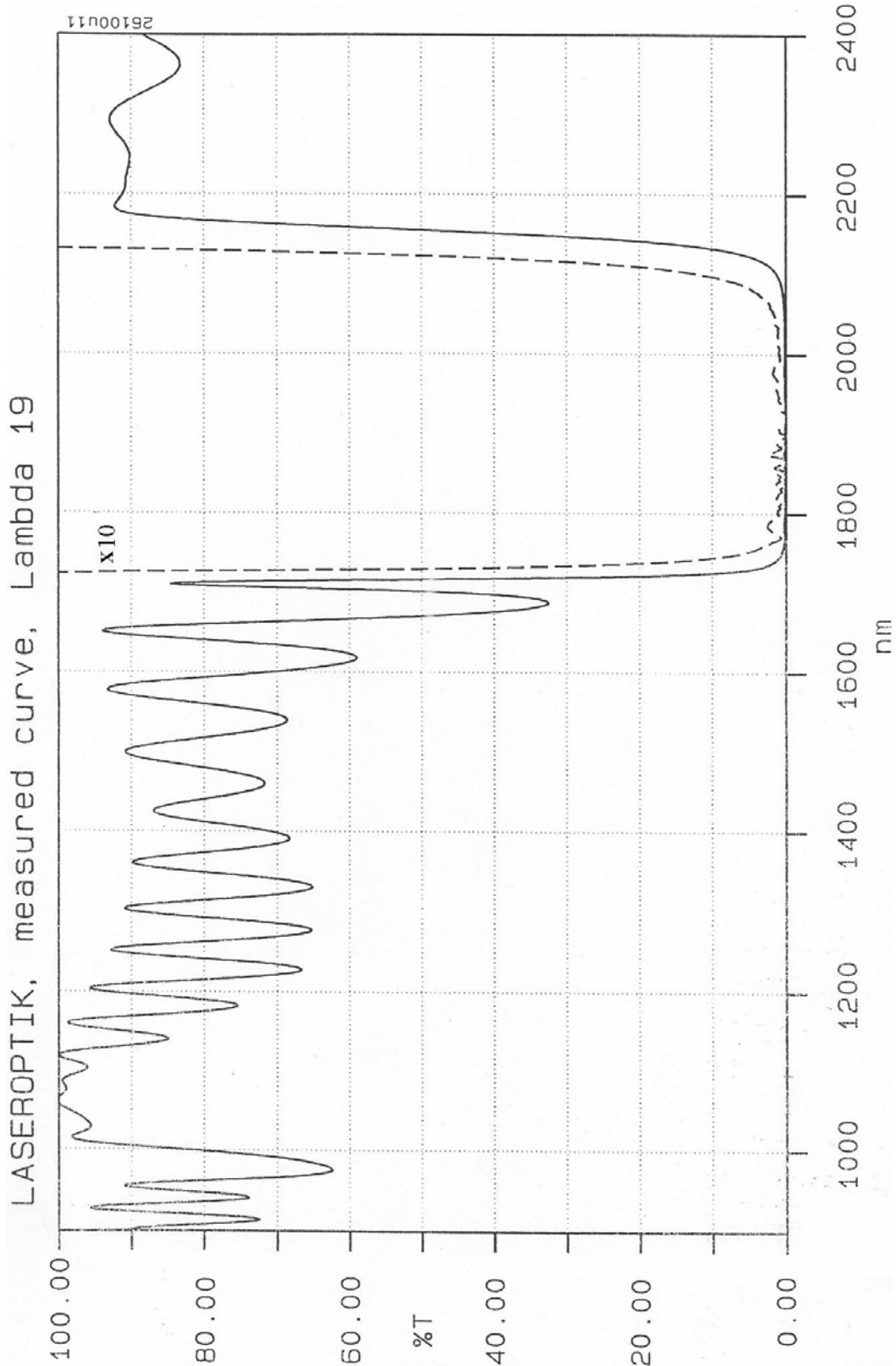


Figure D.1 Frequency response of mirror 1 in the linear OPO. The pump, signal, and idler wavelengths are $1.064 \mu\text{m}$, $2.080 \mu\text{m}$, and $2.173 \mu\text{m}$, respectively.

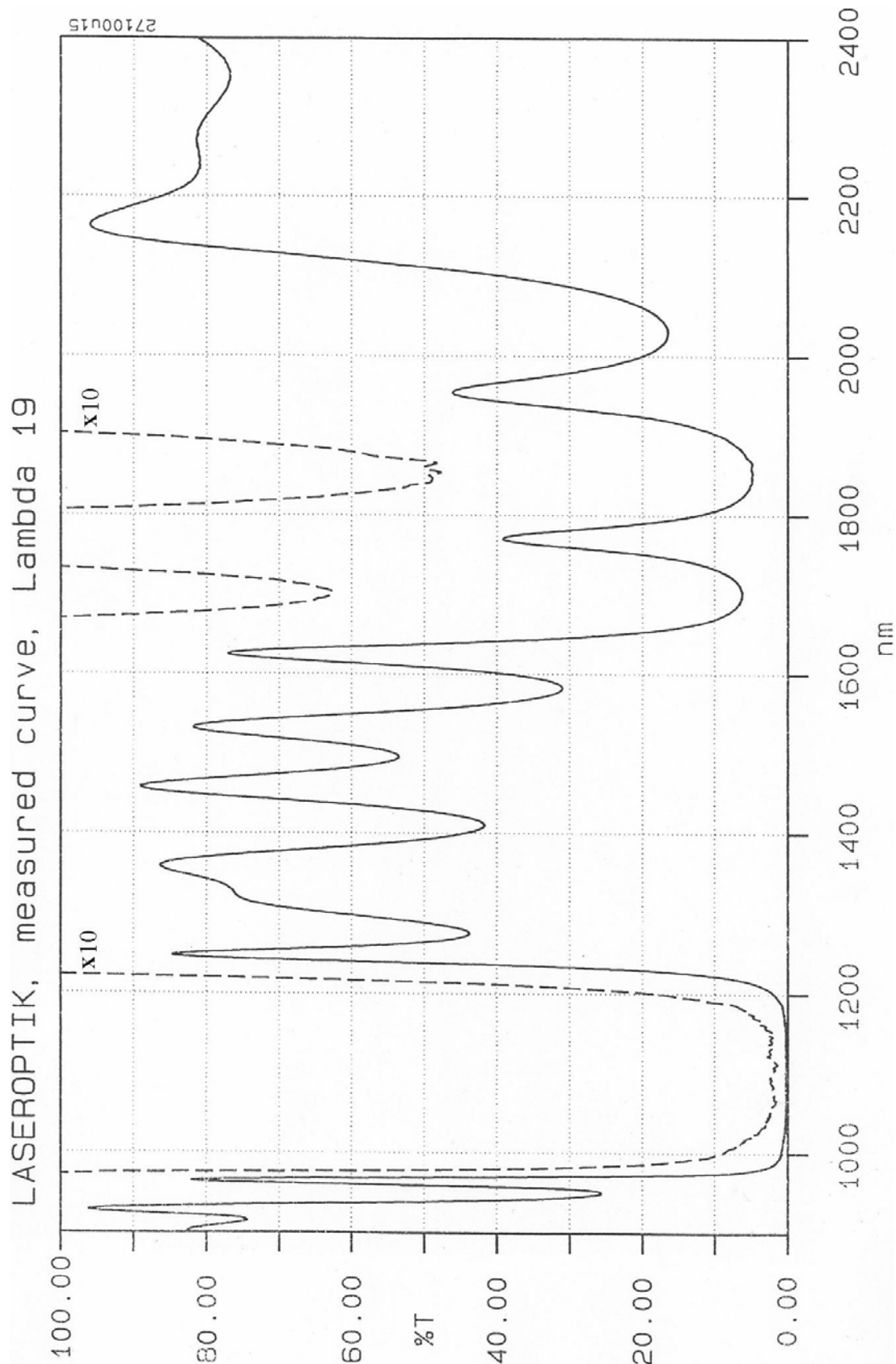


Figure D.2 Frequency response of mirror 2 (the output coupling mirror) in the linear OPO. The pump, signal, and idler wavelengths are 1.064 μm , 2.080 μm , and 2.173 μm , respectively.

References

- [1] S.A. Akhmanov, A.I. Kovrigin, A.S. Piskarskas, V.V. Fadeev, and R.V. Khokhlov (1965). Observation of parametric amplification in the optical range. *JETP Lett.* **2**, 191-193.
- [2] J.A. Giordmaine and R.C. Miller (1965). Tunable coherent parametric oscillation in LiNbO₃ at optical frequencies. *Phys. Rev. Lett.* **14**, 973-976.
- [3] E.C. Cheung, S. Palese, H. Injeyan, C. Hoefer, J. Ho, R. Hilyard, H. Komine, and J. Berg. In: *Advanced Solid State Lasers*, Vol. 26 of Trends in Optics and Photonics Series (Optical Society of America, Washington, D.C., 1999), pp. 514–517.
- [4] J.A.C. Terry, K.J. McEwan, and M.J.P. Payne. In: *Advanced Solid State Lasers*, Vol. 19 of Trends in Optics and Photonics Series (Optical Society of America, Washington, D.C., 1998), pp. 236–239.
- [5] R.W. Boyd. *Nonlinear optics*. Academic Press, San Diego, CA, 1992.
- [6] G. Arisholm and G. Rustad (1997). *A review of theory and materials for optical parametric oscillators in the infrared*. FFI/RAPPORT-97/02589, FFI (Norwegian Defence Research Establishment), Kjeller, Norway.
- [7] J.E. Midwinter and J. Warner (1965). The effects of phase matching method and of uniaxial crystal symmetry on the polar distribution of second-order nonlinear optical polarization. *Brit. J. Appl. Phys.* **16**, 1135-1142.
- [8] B.E.A. Saleh and M.C. Teich. *Fundamentals of Photonics*. John Wiley & Sons, New York, 1991.
- [9] D.J. Armstrong, W.J. Alford, T.D. Raymond, A.V. Smith, and M.S. Bowers (1997). Parametric amplification and oscillation with walkoff-compensating crystals. *J. Opt. Soc. Am. B* **14**, 460-474.
- [10] G.T. Moore and K. Koch. (1995). Efficient High-Gain 2-Crystal Optical Parametric Oscillator. *IEEE J. Quantum Electron.* **31**, 761-768.
- [11] A.E. Siegman. New developments in laser resonators. In: *Optical resonators*, Proceedings of SPIE vol. 1224, (SPIE, Bellingham, WA, 1990), pp. 2-14.
- [12] A.V. Smith and M.S. Bowers (2001). Image-rotating cavity designs for improved beam quality in nanosecond optical oscillators. *J. Opt. Soc. Am. B* **18**, 706-713.
- [13] Ø. Nordseth (2003). *Optical parametric frequency conversion of high energy pulses*. Project report dissertation, NTNU/UniK, Trondheim/Kjeller, Norway.

- [14] J.C. McCarthy, R.C. Day, and E.P. Chicklis. Novel, efficient, high brightness KTP optical parametric oscillator – amplifier in single beamline. In: *Advanced solid-state lasers*, Vol. 50 of Trends in Optics and Photonics Series (Optical Society of America, Washington, D.C., 2001), pp. 656-659.
- [15] G. Anstett, A. Borsutzky, and R. Wallenstein (2003). Investigation of the spatial beam quality of pulsed ns-OPOs. *Appl. Phys. B* **76**, 541-545.
- [16] A. Yariv, *Optical Electronics in Modern Communications*. 5th edition, Oxford University Press, New York, 1997.
- [17] Brilliant - Brilliant B, Instruction manual. Issue #5, 2002. Quantel SA, Les Ulis, France.
- [18] H. Vanherzeele, J.D. Bierlein, and F.C. Zumsteg (1988). Index of refraction measurements and parametric generation in hydrothermally grown KTiOPO₄. *Appl. Opt.* **27**, 3314-3316.
- [19] B. Boulanger, J.P. Fève, and G. Marnier (1997). Absolute measurement of quadratic nonlinearity of phase-matched second-harmonic generation in a single KTP crystal cut as a sphere. *J. Opt. Soc. Am. B* **14**, 1380-1386.
- [20] F. Ahmed (1989). Laser damage threshold of KTiOPO₄. *Appl. Opt.* **28**, 119-122.
- [21] R.P. Jones (1995). Parametric oscillation in KTP and KTA at 1064 nm. Proceedings of SPIE vol. 2379, pp. 357-361.
- [22] International Organization for Standardization. *Lasers and laser-related equipment – Test methods for laser beam parameters – Beam widths, divergence angle and beam propagation factor*, ISO 11146, Geneva, 1999.